Mapping the Conformational Landscape of a Dynamic Enzyme

by Multitemperature and XFEL Crystallography

Daniel A. Keedy[1*], Lillian R. Kenner[1*], Matthew Warkentin[2*], Rahel A. Woldeyes[1*], Jesse B. Hopkins[2], Michael C. Thompson[1], Aaron S. Brewster[3], Andrew H. Van Benschoten[1], Elizabeth L. Baxter[4], Monarin Uervirojnangkoorn[5,6], Scott E. McPhillips[4], Jinhu Song[4], Roberto Alonso-Mori[7], James M. Holton[3,4,8], William I. Weis[5,9,10], Axel T. Brunger[5,6,9,10], S. Michael Soltis[4], Henrik Lemke[7], Ana Gonzalez[4], Nicholas K. Sauter[3], Aina E. Cohen[4], Henry van den Bedem[4#], Robert E. Thorne[2#], James S. Fraser[1#]

1 - Dept. of Bioengineering and Therapeutic Sciences, University of California, San Francisco, San Francisco, CA 94158

2 - Physics Dept., Cornell University, Ithaca, NY 14853

3 - Physical Biosciences Division, Lawrence Berkeley National Laboratory, Berkeley, CA 94720

4 - Stanford Synchrotron Radiation Lightsource, SLAC National Accelerator Laboratory, Menlo Park, CA 94025

5 - Dept. of Molecular and Cellular Physiology, Stanford University, Stanford, CA 94305

6 - Howard Hughes Medical Institute, Stanford University, Stanford, CA 94305

7 - Linac Coherent Light Source, SLAC National Accelerator Laboratory, Menlo Park, CA 94025

8 - Dept. of Biochemistry and Biophysics, University of California, San Francisco, San Francisco, CA 94158

9 - Dept. of Structural Biology, Stanford University, Stanford, CA 94305

10 - Dept. of Photon Sciences, SLAC National Accelerator Laboratory, Menlo Park, CA 94025

Author contributions:

    Prepared Samples: LRK, MW, JSF

    Collected XFEL Data: LRK, RAW, ASB, AHVB, ELB, SEM, JS, RAM, SMS, HL, AG, AEC, HvdB, JSF

    Collected Synchrotron data: MW, JBH, HvdB, JSF

    Processed Data: RAW, ASB, NKS, MCT, AHVB, DAK, MU, JMH, WIW, ATB, AG

    Analyzed Data: DAK, RAW, MCT, HvdB, RET, JSF

    Wrote Paper: DAK, RAW, HvdB, RET, JSF

    Edited Paper: All authors

*equal contributions

#corresponding authors: vdbedem@slac.stanford.edu, ret6@cornell.edu, james.fraser@ucsf.edu

33 **Abstract**

34 Determining the interconverting conformations of dynamic proteins in atomic detail is a major challenge for
35 structural biology. Conformational heterogeneity in the active site of the dynamic enzyme cyclophilin A (CypA)
36 has been previously linked to its catalytic function, but the extent to which the different conformations of these
37 residues are correlated is unclear. Here we compare the conformational ensembles of CypA by multitemperature
38 synchrotron crystallography and fixed-target X-ray free electron laser (XFEL) crystallography. The "diffraction-
39 before-destruction" nature of XFEL experiments provides a radiation-damage-free view of the functionally
40 important alternative conformations of CypA, confirming earlier synchrotron-based results. We monitored the
41 temperature dependences of these alternative conformations with eight synchrotron datasets spanning 100-310 K.
42 Multiconformer models show that many alternative conformations in CypA are populated only at 240 K and
43 above, yet others remain populated or become populated at 180 K and below. These results point to a complex
44 evolution of conformational heterogeneity between 180-240 K that involves both thermal deactivation and
45 solvent-driven arrest of protein motions in the crystal. The lack of a single shared conformational response to
46 temperature within the dynamic active-site network provides evidence for a conformation shuffling model, in
47 which exchange between rotamer states for a large aromatic ring in the middle of the network shifts the
48 conformational ensemble for the other residues in the network. Together, our multitemperature analyses and
49 XFEL data motivate a new generation of temperature- and time-resolved experiments to structurally characterize
50 the dynamic underpinnings of protein function.

Introduction

Current structural biology methods provide only incomplete pictures of how proteins interconvert between distinct conformations (Motlagh et al., 2014; van den Bedem and Fraser, 2015). Although X-ray crystallography reveals atomic coordinates with relatively high accuracy and precision, the resulting electron density maps contain contributions from multiple alternative conformations reflecting the ensemble average of 10^6-10^{15} copies of the protein in one crystal (Rejto and Freer, 1996; Smith et al., 1986; Woldeyes et al., 2014). At high resolution, it is often possible to detect and discretely model these alternative conformations (Burnley et al., 2012; Davis et al., 2006; Lang et al., 2010; van den Bedem et al., 2009). Structural characterization of alternative conformations by X-ray crystallography can complement NMR (Baldwin and Kay, 2009; Fenwick et al., 2014) and computational simulations (Dror et al., 2012; Ollikainen et al., 2013) in defining the structural basis of protein dynamics and ultimately in linking dynamics to function (Henzler-Wildman and Kern, 2007).

However, more than 95% of crystal structures are determined at cryogenic temperatures (~100 K) to reduce radiation damage by minimizing diffusion of reactive intermediates and chemical-damage-induced structural relaxations (Garman, 2010; Holton, 2009; Warkentin et al., 2013). Unfortunately, cryocooling can modify mainchain and sidechain conformational distributions throughout the protein, including at active sites and distal regions important for allosteric function (Fraser et al., 2011; Halle, 2004; Keedy et al., 2014). Recent studies have instead used room-temperature data collection to reveal a multitude of previously "hidden" alternative conformations that are not evident at cryogenic temperatures, many of which have important ramifications for determining molecular mechanisms (Deis et al., 2014; Fraser et al., 2009; Fukuda and Inoue, 2015; Keedy et al., 2014; van den Bedem et al., 2013).

Between these temperature extremes, protein conformational heterogeneity changes in complex ways. Previous studies using a wide variety of biophysical probes including NMR, X-ray crystallography, and neutron scattering have revealed a change in the character of conformational heterogeneity and/or protein dynamics around 180-220 K (Doster, 2010; Lewandowski et al., 2015; Ringe and Petsko, 2003); add Frauenfelder et al., 2009 Doi: 10.1073pnas.0900336106 however, the molecular origins of this "glass" or "dynamical" transition remain incompletely understood. Classic work has examined the temperature dependence of protein conformational heterogeneity across individual X-ray structures determined at temperatures from ~80-320 K (Frauenfelder et al., 1987; Frauenfelder et al., 1979; Tilton et al., 1992). These studies used atomic B-factors as a proxy for conformational heterogeneity and identified a global inflection point around 180-220 K. This inflection point was interpreted in terms of a transition driven by dynamical arrest of the coupled hydration layer-protein system (Frauenfelder et al., 1987; Tilton et al., 1992). Add Doster 2010; Frauenfelder 2009 from above as these are the most detailed presentation of this view. In contrast, solution NMR studies of ps-ns timescale methyl sidechain order parameters showed heterogeneous changes in motional amplitudes at temperatures between 288 K and 346 K. Thermal deactivation of these motions was suggested to predict a transition near 200 K without invoking

87   solvent arrest (Lee and Wand, 2001). Recent solid-state NMR (ssNMR) experiments suggest that protein motions

88   are coupled to solvent, and that three transitions at ~195, 220, and 250 K mark the onset of distinct classes of

89   motions as temperature increases (Lewandowski et al., 2015). Unfortunately, these studies either used globally

90   averaged data (as with ssNMR or neutron scattering) or imprecisely define atomic-level models of conformational

91   heterogeneity (as with B-factors in X-ray crystallography or NMR order parameters), thus preventing an all-atom

92   understanding of the complex temperature response of protein crystals.

93

94   New crystallographic and computational techniques now enable a more detailed investigation of the temperature

95   dependence of protein conformational heterogeneity at the atomic level. First, the program Ringer (Lang et al.,

96   2014; Lang et al., 2010) evaluates low-level electron density traditionally considered noise to uncover statistically

97   significant "hidden" alternative conformations, which may become populated or depopulated as a function of

98   temperature. Second, multiconformer models with explicit alternative conformations of both backbone and

99   sidechain atoms, as created by manual building or the program qFit (van den Bedem et al., 2013; van den Bedem

100   et al., 2009), can account for non-harmonic motions across separate energy wells (encoded by discrete alternative

101   conformations with distinct occupancies and coordinates) and harmonic motions within energy wells (encoded by

102   B-factors). Third, crystallographic order parameters (S^2) weight these harmonic and non-harmonic contributions

103   in a single metric that quantifies the disorder of each residue in a multiconformer model, allowing direct

104   comparison with NMR-determined order parameters (Fenwick et al., 2014). Finally, methodological advances

105   based on the physics of ice formation have enabled variable-temperature crystallographic data collection at

106   temperatures between 300 K and 100 K with modest or no use of potentially conformation-perturbing

107   cryoprotectants (Warkentin et al., 2012; Warkentin and Thorne, 2009). Together, these methods overcome many

108   of the limitations of previous X-ray-based approaches, and will contribute to an integrated view of how protein

109   conformational heterogeneity and dynamics evolve with temperature.

110

111   The human proline isomerase cyclophilin A (CypA) is an excellent model system for deploying these tools to

112   study the structural basis of functional conformational dynamics and, in particular, to use temperature to

113   understand the extent of correlated motions during an enzyme's catalytic cycle. Previous NMR relaxation data for

114   CypA (Eisenmesser et al., 2002; Eisenmesser et al., 2005) indicated a single common exchange process, both in

115   the apo state and during catalysis, for a network of dynamic residues extending from the core to the active site.

116   Room-temperature crystallography later suggested the precise alternative conformations that collectively

117   interconvert during catalysis (Fraser et al., 2009). However, subsequent NMR relaxation experiments of mutants

118   designed to perturb the dynamics suggested that multiple exchange processes occur within this network (Schlegel

119   et al., 2009). Here, we analyze multitemperature synchrotron experiments to examine the temperature-dependent

120   conformational heterogeneity of CypA. Additionally, we report X-ray free electron laser (XFEL) data, which are

121   free of conventional radiation damage (Kern et al., 2014; Spence et al., 2012), to validate previous connections

122   between alternative conformations determined by synchrotron crystallography and NMR experiments performed

123 in solution (Eisenmesser et al., 2005; Fraser et al., 2009). Computational analysis shows that the temperature

124 dependence of alternative protein conformations is heterogeneous and that the character of this heterogeneity

125 bridges previous models for protein dynamical transitions. Our results suggest new ways to use variable

126 temperature with both synchrotron and XFEL crystallography to probe the dynamic underpinnings of protein

127 function.

128

129 **Results**

130

131 *Multitemperature X-ray Datasets Reveal Modulated Conformational Ensembles of CypA*

132

133 To probe the conformational landscape of CypA, we collected eight high-resolution (1.34-1.58 Å) synchrotron

134 crystallographic datasets across a wide range of temperatures from 100-310 K (**Table 1**) with no added

135 cryoprotectants. For each dataset, we initially refined single-conformer models. Although the single-conformer

136 models are very similar to each other, the accompanying electron density maps reveal differences throughout the

137 protein. In the active-site network, the mFo-DFc difference electron density maps are relatively featureless below

138 200 K, suggesting that a single conformation is a valid fit below this temperature. By contrast, positive and

139 negative mFo-DFc peaks become gradually more prevalent as temperature increases above 200 K, suggesting that

140 multiple conformations are increasingly required to explain the data as temperature increases (**Table 1 – Figure**

141 **S1**).

142

143 We monitored the shift from single-conformation to multiple conformations both visually (**Figure 1 A,B**) and

144 using the automated electron-density scanning program Ringer (**Figure 1 C,D**). Briefly, Ringer identifies

145 alternative conformations at low levels of electron density by evaluating the density value for the γ atom at each

146 possible position about the χ1 dihedral angle, given a fixed mainchain conformation (Lang et al., 2014; Lang et

147 al., 2010). We focused on two residues, Ser99 and Leu98, which are key markers of the conformational exchange

148 by NMR (Eisenmesser et al., 2002; Eisenmesser et al., 2005) and were implicated in our previous room-

149 temperature X-ray and mutagenesis experiments (Fraser et al., 2009). For both Ser99 (**Figure 1 A**) and Leu98

150 (**Figure 1 B**), a dominant peak is evident at all temperatures. The reduced height of this peak as temperature

151 increases is accompanied by the increase in a secondary peak corresponding to the electron density of the minor

152 conformation. To quantify this trend, we computed correlation coefficients between the electron density vs.

153 dihedral angle curves for each residue (**Figure 1 C,D**). Pairs of curves for similar temperatures have higher

154 correlations than those for different temperatures. In particular, pairs of curves for temperatures that span the low-

155 temperature (100-180 K) and high-temperature (240-310 K) regimes are more poorly correlated than are curves

156 from the same temperature regime. the dynamical transitions observed in previous studies (Doster, 2010; Lee and

157 Wand, 2001; Lewandowski et al., 2015; Ringe and Petsko, 2003) generally occur between these two temperature

158 regimes.

159

160   To ground this conformational redistribution in all-atom detail, we built a multiconformer model with qFit (van

161   den Bedem et al., 2013; van den Bedem et al., 2009) for each multitemperature dataset. We then finalized the

162   model by manually editing alternative conformations and refining to convergence, resulting in models that were

163   improved relative to the single-conformer models (**Table 2**, **Movie 1**). At 180 K and below, the active-site

164   network is best modeled as a single state, with electron density corresponding to ordered water molecules clearly

165   evident adjacent to Phe113 (**Figure 2**, top row). At 240 K and above, by contrast, multiple conformations provide

166   a better explanation of the data. Interestingly, some partial-occupancy water molecules are still present and likely

167   co-occur with the major conformations (**Figure 2**, middle and bottom rows). Met61 appears to populate additional

168   conformations above 180 K, although it is difficult to precisely define changes in its conformational ensemble as

169   temperature increases. This residue bridges Phe113 and the catalytic residue Arg55 via steric contacts between

170   alternative conformations in both directions, emphasizing the importance of modeling multiple conformations in

171   all-atom detail for understanding inter-residue coupling.

172

173   *XFEL Data Confirm Conformational Heterogeneity in Synchrotron Data Is Not Due to Radiation Damage*

174

175   Quantifying radiation damage versus exposure dose (**Table 1 – Figure Supplement 2**) and limiting exposure

176   dose per dataset ensured that the conformational heterogeneity observed in multitemperature synchrotron datasets

177   was not dominated by radiation damage. However, XFELs can generate data that is entirely free from

178   conventional radiation damage by "diffraction before destruction" data collection (Kern et al., 2014; Spence et al.,

179   2012). To compare the distribution of alternative conformations between synchrotron and XFEL data, we

180   collected two ambient-temperature datasets: a 1.75 Å resolution radiation-damage-free dataset using serial

181   femtosecond rotation crystallography (**Table 3**) (Hirata et al., 2014; Schlichting, 2015; Suga et al., 2015) and an

182   additional 1.2 Å resolution synchrotron dataset (**Table 4**). For the XFEL experiment, we collected 1,239

183   individual frames, translating to unique unexposed regions of 71 crystals between each shot (**Movie 2**), and

184   processed them using cctbx.xfel (Hattne et al., 2014) with post-refinement in PRIME (Uervirojnangkoorn et al.,

185   2015). Automated molecular replacement yielded interpretable electron density maps that allowed us to refine a

186   single-conformer structural model with reasonable quality statistics. Electron-density sampling analysis using

187   Ringer and multiconformer refinement using qFit were performed as for the multitemperature synchrotron data.

188

189   In agreement with our previous room-temperature studies (Fraser et al., 2009), the XFEL and synchrotron mFo-

190   DFc difference maps reveal evidence for the rate-limiting alternative conformations extending from the active site

191   into the core of the protein (**Figure 3 A,B**). For example, the backrub-coupled (Davis et al., 2006) rotamer jump

192   of Phe113 is apparent from a large positive mFo-DFc peak in both maps. Alternative conformations for core

193   residue Ser99 are also evident from mFo-DFc peaks (**Figure 3 A,B**) and Ringer electron-density sampling curves

194   (**Figure 3 E**). We did not conclusively observe a Ringer peak for a discrete alternative conformation of Leu98

195   (**Figure 3 F**), but that is likely due to the lower resolution of the XFEL dataset. Multiconformer models for both

196   datasets (**Figure 3 C,D**) again feature alternative conformations across the active-site network and are strongly

197   supported by 2mFo-DFc electron density. These results provide an important positive control on the observation

198   of conformational heterogeneity in our synchrotron studies by establishing that electron density corresponding to

199   the alternative conformations of CypA is not an artifact of radiation damage. The ability of XFEL crystallography

200   to reveal native and functionally important alternative conformations at high resolution may be especially useful

201   for other systems that are presently intractable for room- or variable-temperature synchrotron crystallography due

202   to the small size of available crystals.

203

204   *Some Regions Feature Conformational Heterogeneity Only At Low Temperatures*

205

206   Although more conformational heterogeneity is expected with our higher-temperature synchrotron datasets, and is

207   evident in the active site of CypA, cooling can also stabilize new conformations (Halle, 2004). For example, the

208   loop containing residues 79-83 (**Figure 4**, **Movie 3**) exhibits conformational heterogeneity only at cryogenic

209   temperatures. This region is well fit by a single conformation at 240 K and above, but a secondary loop

210   conformation is necessary to explain the electron density at 100, 150, and 180 K. Additionally, the loop is clearly

211   single-state in the highest-resolution (1.2 Å) dataset (**Figure 4 - Figure S1**), demonstrating that the slightly lower

212   resolution of the elevated-temperature datasets does not obscure a secondary conformation.

213

214   In the primary conformation, the 79-83 loop is not involved in any mainchain-mainchain hydrogen bonds to the

215   rest of CypA, suggesting that the barrier to forming the secondary conformation does not involve breakage of

216   cooperative secondary-structure-like interactions. The observation of a secondary state for residues 79-83 at 100-

217   180 K, but not at 240-310 K, suggests that it is enthalpically stabilized at lower temperatures (Halle, 2004; Keedy

218   et al., 2014). Consistent with this mechanism, the secondary conformation of the 79-83 loop is accompanied by an

219   ordered, partial-occupancy water molecule (**Figure 4**, top row). This water molecule, which is clearly distinct

220   from the carbonyl oxygen of the primary conformation of Glu81, wedges between the loop and the rest of the

221   protein. The surprising appearance of specific solvent-linked protein conformational heterogeneity exclusively

222   below 240 K emphasizes the complex and heterogeneous changes in protein-solvent energetics that can occur at

223   cryogenic temperatures.

224

225   *Quantifying Temperature-Dependent Changes in Conformational Heterogeneity*

226

227   Despite counterexamples such as the 79-83 loop, most residues in CypA, especially in the active site, exhibit

228   increases in discrete conformational heterogeneity above 180 K. To quantify these changes in regions implicated

229   by NMR relaxation experiments, we measured the 2mFo-DFc electron density in the volumes occupied by the

230   alternative conformations of Ser99 and Phe113. In contrast, B-factors, which can model the harmonic motions

231   near any single conformation, are poor proxies for the non-harmonic change between discretely separated

232   conformations. To quantify the change in minor state occupancy as a function of temperature, we summed the

233   electron density in the volume that is occupied exclusively by the minor conformation, and avoided any voxels

234   that overlap with the van der Waals radii of atoms of the major conformation (**Figure 5 A**). The resulting curves

235   of minor-state electron density vs. temperature have a shallow slope at 180 K and below, but a much steeper slope

236   at 240 K and above (**Figure 5 B,C**). Additionally, the electron density for the XFEL data is consistent with the

237   data collection temperature (273 K) and the overall trends.

238

239   However, most residues that populate alternative conformations do not have such easily characterized and

240   separable regions of electron density. To quantify how conformational heterogeneity throughout CypA varies as a

241   function of temperature, we used B-factor-dependent crystallographic order parameters (S^2) (Fenwick et al.,

242   2014). These order parameters include both harmonic contributions, which reflect conformational heterogeneity

243   near one conformation (encoded by B-factors), and non-harmonic contributions, which reflect conformational

244   heterogeneity between multiple discretely separated conformations (encoded by occupancies and displacements in

245   coordinates). Importantly, these order parameters account for both conformational heterogeneity within energy

246   wells, whether it is modeled by B-factors or by subtly different alternative conformations, as well as discretely

247   separated alternative conformations that occupy distinct rotamers. Similar to the 2mFo-DFc electron density

248   integration results for Phe113, we observed a large change in $\chi 1$ bond order parameters at 240 K and above

249   (**Figure 6 A**).

250

251   *Mapping the Transitions in CypA Conformational Heterogeneity*

252

253   Next, we applied the order parameter analysis to all sidechain $\chi 1$ angles in CypA. Although conformational

254   heterogeneity generally increases with temperature throughout the enzyme, we observed a diverse set of

255   conformational responses (**Figure 6 – Figure S1**). The trends for the majority of residues suggested a transition

256   somewhere between our data points at 180 and 240 K, below which the change in conformational heterogeneity

257   with temperature is reduced. To quantify this trend, we performed separate fits for the low-temperature (≤180 K)

258   and high-temperature (≥240 K) data points for all residues. The slopes of conformational heterogeneity (1-S^2) vs.

259   temperature were significantly different (p=1×10^{-62}, paired T-test) on either side of this transition range: the

260   average slope for the low-temperature fit lines (2.5×10^{-4} K^{-1}) was an order of magnitude smaller than for the high-

261   temperature fit lines (2.6×10^{-3} K^{-1}). This is consistent with the idea that heterogeneity is much less dependent on

262   temperature below the 180-240 K "transition" range.

263

264   However, some residues behaved differently from the rest of the protein. Val2 retains its conformational

265   heterogeneity at all temperatures, which is expected based on its weakly constrained position at the N-terminus.

266   Many of the remaining outlier residues (Glu15, Glu81, Pro105, Ala117, Glu120, Lys125, Met142, Ser147,

267   Lys151) appear to be involved in a spatially contiguous set of crystal contacts across symmetry mates in the

268   context of the crystal lattice (**Figure 6 - Figure S2**). This cluster includes Glu81, which adopts alternative

269   backbone conformations only at low temperatures (**Figure 4**). The variability of these residues can likely be

270   explained by distinct sets of conformations across crystal contacts that are differentially, but somewhat

271   stochastically, favored during the cooling process (Alcorn and Juers, 2010).

272

273   Our data suggest that CypA does not undergo a single global transition from having strongly temperature-

274   dependent changes in sidechain conformational heterogeneity to relatively temperature-independent behavior. An

275   "intersection" or "transition" temperature for each bond angle can be estimated from the intersection of the low-

276   temperature and high-temperature fit lines of $1-S^2$ versus temperature. The distribution of these intersection

277   temperatures is broad and asymmetrical, with an elongated tail from the peak near 250 K toward 200 K (**Figure 6**

278   **B**). Furthermore, the distribution of intersection temperatures is more complex for order parameters reporting on

279   the terminal heavy-atom bond of the sidechain than for $\chi 1$ (**Figure 6 - Figure S3**, **Figure 6 - Figure S4**). This

280   increase likely occurs because sidechain end orientations are subject to more degrees of freedom and therefore

281   temperature changes may redistribute them in a greater variety of ways.

282

283   *Distinguishing Between Models of Protein Heterogeneity as a Function of Temperature*

284

285   Our data provide insight into models for the origin of the temperature dependence of protein conformational

286   heterogeneity and into proposed dynamical transitions. In one model, deactivation of different internal protein

287   motions at high temperatures (near 300 K) is sufficient to predict a dynamical transition near 200 K (Lee and

288   Wand, 2001). In a second model, solvent-coupled arrest of protein motions produces a transition in a similar

289   temperature range (Ringe and Petsko, 2003). To distinguish between these two models, we analyzed the average

290   sidechain disorder across all residues in CypA, focusing on the bond most closely associated with the $\chi 1$ dihedral

291   angle, at each of the eight temperatures we studied (**Figure 6 C**). These averaged disorder values drop as

292   temperature is decreased from 310 K, then flatten out somewhere between 240 and 180 K, with some scatter due

293   to the variability in the cryocooling process (data points in **Figure 6 C**, **Figure 6 – Figure Supplement 7**).

294

295   Next, we used two different linear fits to extrapolate $1-S^2$ across all temperatures for each residue, floored the

296   result at maximum order ($1-S^2=0$), and then averaged across all residues to obtain predictions for the residue-

297   averaged disorder versus temperature. In the first fit, the linear function was fit to data for each residue at all

298   temperatures. Consistent with the necessity of using separate fit lines for the low-temperature and high-

299   temperature data (**Figure 5** and **Figure 6 – Figure S1**), the resulting prediction gives a poor account of the

300   averaged experimental data and does not indicate a transition (purple line in **Figure 6 C**). In the second fit, only

301   the high temperature (240 K and above) data for each residue was fit. The resulting prediction is more consistent

302   with the averaged high-temperature experimental data, and does indicate a transition (red line in **Figure 6 C**). The

303 flattening of this predicted curve at low temperatures occurs as more individual residues achieve maximal

304 predicted order ($S^2 \rightarrow 1$) (**Figure 6 - Figure S5**). This latter prediction, which is extrapolated from high-

305 temperature crystallographic data, is reminiscent of predictions based on NMR relaxation experiments conducted

306 at 288-346 K (Lee and Wand, 2001). Our observations are consistent with the idea that thermal depopulation of

307 protein alternative conformations is sufficient to predict the existence of an average inflection without invoking a

308 transition of the solvent. However, the low temperature of the predicted inflection (~100 K), as well as the large

309 separation in low-temperature disorder between our experimental data (data points in **Figure 6 C**) and predictions

310 from high temperature (red line in **Figure 6 C**), suggest that thermal depopulation of protein alternative

311 conformations cannot by itself account for the observed ~200 K transition.

312

313 This large separation also indicates that data collected at high temperatures (>260 K) cannot be reliably

314 extrapolated to predict conformational heterogeneity and features of the energy landscape that may be important

315 below ~200 K.

316

317 Many effects may contribute to the discrepancy between the observed data and the behavior projected from the

318 high-temperature fits. To gain additional insight into this discrepancy, we decomposed the order parameters into

319 their B-factor vs. discrete-conformers components and examined their temperature dependences (**Figure 6 –**

320 **Figure S6**). Roughly 67% of residues (e.g., Phe8) remain within one rotamer well across all temperatures.

321 Approximately 13% of residues (e.g., Ser99 and Phe113) populate clearly separable multiple rotameric states at

322 high temperatures, and then show complete depopulation of minority states on cooling so that only a single

323 rotameric state remains at 180 K and below. However, 6% of residues (e.g., Thr5) continue to populate multiple

324 rotameric states at or below 180 K. An additional 6% of residues (e.g., Lys91) populate new rotameric states only

325 at or below 180 K. These results help explain the excess residual disorder in our experimental structures below

326 240 K compared to projections based on high-temperature fits. Although slopes of crystallographic B-factors with

327 temperature remain nearly flat below 240 K (**Figure 6 - Figure S2 B**), we expect that true harmonic thermal

328 disorder does subtly decrease from 180 to 100 K; these thermal effects could be more detectable in higher

329 resolution data from more ordered crystals??

330

331 *Imperfect Coupling Between Active-Site Residues in CypA*

332

333 While the results above show a variety of thermal and non-thermal conformational responses, it remains unclear

334 whether these responses involve coupled conformational shifts of multiple residues. In particular, the network of

335 alternative sidechain conformations spreading from the core of the protein (Ser99) into the active site (Arg55)

336 across multiple β-strands exhibits qualitatively similar behavior of increasing occupancy above 240 K. In previous

337 work (Fraser et al., 2009), the collective presence of these alternative conformations at room temperature, but not

338 at cryogenic temperatures, and the close contacts between these residues had suggested a concordance to the

339 single exchange process fit by NMR relaxation dispersion for this dynamic active-site network. However, using

340 our new multitemperature data, this network appears subdivided based on the apparent intersection or transition

341 temperatures of the constituent residues, with Ser99 and Phe113 behaving most similarly to each other (**Figure 7,**

342 **Movie 4**).

343

344 **Discussion**

345

346 Here we have mapped the conformational landscape of the dynamic enzyme CypA by analyzing multiconformer

347 models from multitemperature crystallography. Unlike previous temperature-dependent analyses of X-ray

348 crystallography, here we consider both harmonic disorder (B-factors) and non-harmonic displacements

349 (alternative conformations and occupancies), characterized using crystallographic bond order parameters. We

350 have four primary findings: (1) The occupancy of alternative sidechain conformations present at 310 K generally

351 decreases with decreasing temperature. (2) However, some residues adopt alternative conformations only at 180 K

352 and below. (3) The temperature response of residues is highly heterogeneous: the "intersection temperature"

353 below which sidechain conformational heterogeneity remains nearly constant has a broad distribution across the

354 molecule, with a peak near 250 K. (4) Residues composing a dynamic active-site network that is important for

355 function do not have a consistent intersection temperature.

356

357 Our results provide new insight into the relationship between energy landscapes, the glass transition, and protein

358 function. Glasses and other disordered systems have complex energy landscapes, in part due to the large number

359 of microenvironments and the extensive frustration that disorder generates in the intermolecular interactions.

360 Proteins at biological temperatures are "glassy" in this sense – they have complex energy landscapes, due to their

361 large size, heterogeneous amino acid composition, extensive frustration, and many degrees of conformational

362 freedom (Frauenfelder et al., 1991; Onuchic et al., 1997; PMID: 9348663 Ferreiro et al., 2014). Doi:

363 10.1017/S0033583514000092

364 The extensive heterogeneity in the temperature response of individual residues in CypA we observe here

365 provides additional direct evidence for this underlying energetic heterogeneity.

366

367 In addition to the inherent "glassiness" of proteins at biological temperatures, early Mossbauer and

368 crystallographic work suggested a collective "glass transition" near 200 K associated with hydration solvent –

369 protein coupling. Glass transitions are by definition non-equilibrium phenomena that arise when the kinetics of

370 relaxation toward equilibrium slow so dramatically that equilibrium cannot be reached on experimental

371 timescales. One signature of a true glass transition in proteins would be if occupancies of minority conformations

372 were arrested at non-zero values below some temperature. Indeed, here we see no appreciable temperature

373 evolution of individual conformer occupancies or B-factors at 180 K and below, and the average disorder at these

374 temperatures is far in excess of what is predicted from high-temperature extrapolations. These observations are

375 consistent with the falling out of equilibrium expected in a glass transition, but not with a transition driven by the

376   thermal freeze-out of alternative sidechain conformations (Lee and Wand, 2001). Moreover, the persistence of

377   multiple rotameric states at low temperatures is consistent with solvent arrest that impedes further changes in

378   sidechain disorder.

379

380   Subsequent temperature-dependent studies of proteins by liquid and solid-state NMR, neutron scattering, and

381   other techniques have identified "dynamical transitions" at temperatures including , 180, 195, 220, 240, and 250

382   K (Lewandowski et al., 2015; Schiro et al., 2015). These transitions typically manifest as a change in slope of

383   some measurement in the vicinity of the suggested transition temperature. However, many of these measurements

384   are sensitive to motions only within some timescale window (often ps-ns), monitor only a subset of amino acid

385   types, and/or spatially average over all residues in the protein. By contrast, multitemperature crystallography with

386   multiconformer models has many advantages by providing a time-independent and fully site-resolved

387   measurement of ensemble-averaged atomic displacements, including both harmonic and discrete conformational

388   heterogeneity, within the crystal.

389

390   The critical importance of site resolution is evident in the results of Figure 6. Averaging over sidechain disorder

391   in all residues yields an apparent transition near 250 K (**Figure 6** and **Figure 6 - Figure S7**). Perhaps

392   coincidentally, this same temperature has been associated with a transition for protein sidechains in site-averaged

393   solid-state NMR measurements (Lewandowski et al., 2015). However, the "transition" in our residue-averaged

394   result obscures the highly heterogeneous temperature dependence of the individual sidechains. We find no

395   evidence of tight cooperativity or of a collective global response near 250 K that would be expected in the case of

396   a "true" dynamical transition Instead, our data are consistent with alocal, non-cooperative freeze-out of

397   conformational states defined by the energy landscape over a broad temperature range.

398

399

400   The heterogeneous response of side chain order parameters to temperature is driven largely by the changes to the

401   populations of alternative conformations, which "flat-line" at different temperatures across CypA. This diversity

402   of "flat-lining" temperatures is present even within the dynamic active-site network, even though the constituent

403   residues have similar occupancies for their major and minor states at high temperatures (**Figure 7**). This result

404   contrasts with previous NMR and X-ray experiments that hypothesized correlated motions of this network as rate-

405   limiting for the catalytic cycle (Eisenmesser et al., 2005; Fraser et al., 2009) (**Figure 8 A**). To bridge these views,

406   we propose that the active-site network adopts two substates, which are primarily distinguished by Phe113

407   rotamer interconversion. Each of these substates adopts a differently weighted ensemble of conformations for

408   other residues (**Figure 8 B**). In this model, Met61 and Arg55 can switch rotamers more easily than Ser99 when

409   Phe113 is in its $\chi1$ gauche+ (p) rotamer pointed toward Ser99, whereas Ser99 can switch rotamers more easily

410   than Met61 and Arg55 when Phe113 is in its $\chi1$ gauche- (m) rotamer pointed toward Met61. Additionally, thermal

411   "breathing" motions within rotameric wells may relieve minor steric overlaps within some of these macro- and

412 microstates (**Figure 8 B**, bottom right). This model is consistent with Phe113 having the lowest "flat-lining"

413 temperature of the network (**Figure 7**), and makes sense sterically because of the large size of the aromatic ring.

414 These hypothesized motions are consistent with the timescales and temperature dependencies of motion assigned

415 by solid-state NMR studies of crystalline protein GB1 (Lewandowski et al., 2015). Furthermore, the model helps

416 explain the difficulty of fitting NMR relaxation data for perturbed versions of the active-site network as a single

417 collective exchange process (Schlegel et al., 2009). The aromatic ring of Phe113 could play a dominant role in

418 determining the chemical shift changes of the surrounding residues. Each of these residues could also populate

419 multiple rotamers in the excited state measured by NMR. Our hierarchical perspective evokes the "population

420 shuffling" model of (Smith et al., 2015), in which a protein macrostate (in CypA, defined by the Phe113 rotamer)

421 is defined by different relative populations of rotamers for a subset of residues (in CypA, the other residues in the

422 active-site network). In this model, the interconversion between these macrostates, and not the collective motion

423 of all residues between distinct rotamers, is correlated with the rate-limiting step of the CypA catalytic cycle.

424

425 Diversity in the temperature dependences of alternative conformations as we see here is inevitable given the

426 diversity and limitations of the amino acid alphabet, yet its spatial pattern within a protein may provide insight

427 into selective pressures. Evolutionary optimization must ensure that functionally important alternative

428 conformations are robustly populated and interconvert appreciably at physiological conditions. However, the

429 energy landscapes of individual residues are coupled to varying extents, such that some subsets of residues must

430 be collectively optimized to preserve some, but not perfect, collectivity in functional motions. For proteins with

431 large sequence alignments, evolutionary covariation has been used to predict "sectors" of functionally cooperative

432 residues, which are often dispersed in primary sequence but strikingly contiguous in tertiary structure (Halabi et

433 al., 2009). Temperature-dependent crystallography has the potential to unveil couplings in atomic detail,

434 includingby identifying sets of residues whose conformational ensembles respond concertedly to temperature

435 change. Based on our results with CypA, we expect this coupling to be weak but measurable.. Serial femtosecond

436 XFEL crystallography combined with ultra-fast temperature jumps will enable a temporal view of these coupled

437 conformational changes. Novel static and time-resolved multitemperature crystallography-based approaches will

438 provide powerful tools for resolving concerted motions to explore how proteins function and evolve.

Methods

Protein expression, purification, and crystallization.
Wildtype CypA was produced and crystallized as previously reported (Fraser et al., 2009). Briefly, crystals were grown by mixing equal volumes of well solution (100 mM HEPES pH 7.5, 23% PEG 3350, 5 mM TCEP) and protein (60 mg mL^{-1} in 20 mM HEPES pH 7.5, 100 mM NaCl, 0.5 mM TCEP) in the hanging-drop format.

Crystallographic data collection.
For the multitemperature synchrotron datasets at 100, 150, 180, 240, 260, 280, 300, and 310 K, we collected data at the Cornell High Energy Synchrotron Source (CHESS) at beamline A1 with a 100 micron collimator using a wavelength of 0.9767 Å. Crystals were looped by hand, stripped of excess mother liquor (100 mM HEPES pH 7.5, 23% PEG 3350, 5 mM TCEP) using NVH oil (Warkentin and Thorne, 2009), and placed directly into the nitrogen-gas cryostream pre-set to the desired temperature at the beamline. Water inside protein crystals is nanoconfined so that ice nucleation is dramatically suppressed, but water outside crystallizes readily and rapidly. Careful removal of all excess solvent from the crystal surface is essential to obtaining ice-free diffraction between 260 K and 180 K without using large cryoprotectant concentrations.

For the XFEL experiment, we collected multiple diffraction images per crystal using a 10 micron X-ray beam with each irradiation point separated by at least 25-40 microns to avoid collateral radiation damage. A total of 1,239 still diffraction images were collected from 71 CypA crystals over the course of two experiments using a goniometer setup and a Rayonix MX325HE detector at LCLS-XPP (Cohen et al., 2014) (**Movie 1**). All data was collected at ambient temperature (approximately 273 K). To prevent dehydration, crystals were coated with paratone oil immediately after looping and mounted on the goniometer at the XPP end station of LCLS using the SAM sample exchange robot (Cohen et al., 2002).

For the new 1.2 Å room-temperature synchrotron dataset, paratone oil was applied to cover a 2 µL hanging drop containing a single large crystal of CypA. The crystal was harvested through the paratone and excess mother liquor was removed using a fine paper wick. Attenuated data was collected at SSRL beamline 11-1 at 273 K controlled by the cryojet on the PILATUS 6M PAD detector.

Crystallographic data processing.
The synchrotron datasets were indexed, integrated, and scaled using XDS and XSCALE, and intensities were subsequently converted to structure factor amplitudes using XDSCONV. All datasets were from single crystals. Data reduction statistics for the highest-resolution room-temperature dataset and the multitemperature datasets can be found in **Table 4** and **Table 1,** respectively.

The XFEL data were processed using *cctbx.xfel* (Hattne et al., 2014). Of the 1,239 images collected, 772 were indexed and their intensities were integrated. Post-refinement, as implemented by *PRIME* (**p**ost-**ref**inement and **me**rging, version date: Nov 11 20:22:51 2014)(Uervirojnangkoorn et al., 2015), was used to correct the intensity measurements and merge the data. We optimized over the uc_tolerance, n-postref_cycle, sigma_min, partiality_min, and gamma_e values to obtain the final structure factor amplitudes. Data reduction statistics for the XFEL data are provided in **Table 3**.

To promote consistency between models derived from different data sets, R$_{free}$ flags were generated using *PHENIX* for the highest-resolution "reference" (1.2 Å 273 K) dataset first, and were subsequently copied to all other multitemperature and XFEL datasets for the automated molecular replacement and refinement pipeline.

486 *Model building.*
487 For each dataset, we calculated initial phases by performing molecular replacement with *phenix.auto_mr* using
488 PDB ID 2cpl as a search model. We next refined XYZs and ADPs of the initial model with *phenix.refine* for 4
489 macrocycles with XYZ and ADP weight optimization turned on; identified TLS groups with
490 *phenix.find_tls_groups*; and refined optimized XYZs, ADPs, and TLS parameters for 6 more macrocycles. These
491 single-conformer models and associated electron density maps were used as input for two subsequent steps.
492
493 First, the single-conformer models were analyzed with Ringer (Lang et al., 2010) via *mmtbx.ringer* using default
494 settings. A coupled sidechain-backbone "backrub" motion (Davis et al., 2006) of -10° for Ser99 (see **Figure 5A**)
495 was necessary to match the Cα and Cβ positions of the minor conformation as modeled in PDB ID 3K0N; using
496 this modified backbone indeed yielded maximal minor-conformation Ringer peaks for our multitemperature
497 datasets. No backrub motion was necessary for Leu98 due to the different type of backbone displacement (Fraser
498 et al., 2009). Correlation coefficients between pairs of Ringer curves were calculated using the *cor* function in R
499 (Team, 2014).
500
501 Second, the single-conformer models were used as input to *qFit* (Keedy et al., 2014; van den Bedem et al., 2009).
502 Subsequent to the automated model building, we manually deleted ill-fitting waters and edited alternative protein
503 sidechain conformations based on fit to the electron density in *Coot* (Emsley et al., 2010) and refinement with
504 *phenix.refine*. For example, at 240 K, *qFit* automatically modeled Phe113 as single-state, but significant +mFo-
505 DFc peaks remained, so we decided on a two-state model. Met61 was particularly difficult to model accurately
506 across temperatures due to convolved issues of $\chi 3$ non-rotamericity for Met in general (Butterfoss et al., 2005),
507 the relatively high electron count for sulfur, and likely temperature-modulated Met-specific radiation damage. For
508 these reasons, visual inspection of the maps and manual building is currently essential for alternative backbone
509 conformations with moderate displacements, as observed in residues 79-83 (**Figure 4**). We are currently
510 developing new methods to automatically detect and model such backbone excursions in multiscale
511 multiconformer models. These efforts improved R_{free} and MolProbity scores across datasets (**Table 2**). Because of
512 the lower resolution, the XFEL model was refined with three TLS groups and with optimization of X-ray vs.
513 geometry and ADP weights.
514
515 *Model and electron density analysis.*
516 For minor-state electron density sums, 2mFo-DFc (Fc filled) map values were summed across a grid of points
517 defined by superimposing each model onto PDB ID 3k0n using all Cα atoms, summing the 2mFo-DFc value at
518 each point with 0.25 Å of a target minor-state heavy atom (Oγ for Ser99; Cδ1, Cε1, Cε2, or Cζ for Phe113), and
519 normalizing to unity across datasets for each residue being analyzed. This procedure allowed a strictly common
520 reference set of map evaluation points. Results were very similar when using unfilled maps (data not shown).
521
522 We calculated B-factor-influenced order parameters (S^2) as previously reported (Fenwick et al., 2014) except that
523 we monitored one of two different types of bond vector. For the $\chi 1$ order parameter, we used Cβ-Xβ (where X =
524 C or O) for most amino acids, Cα-Cβ for Ala, and Cα-Hα for Gly. For the sidechain-end order parameter, we used
525 the heavy-atom to heavy-atom bond vector for each amino acid that was closest to the sidechain terminus, with
526 ties broken by the number in the atom name (e.g. Cγ-Cδ1 instead of Cγ-Cδ2 for Leu). All negative order
527 parameters (caused by high B-factors) were floored to 0. $\chi 1$ order parameters were floored for 7 residues, and
528 sidechain-end order parameters were floored for 23 residues. Per-residue "apparent dynamic transition
529 temperatures" were then calculated as the intersection between the <200 K and >200 K fit lines in order parameter
530 vs. temperature plots and floored to 0 K if necessary. The kernel density curve was fit with the *density* function in
531 R (Team, 2014).
532

533   For extrapolation of fit lines in **Figure 6**, we used a fit to all data points or to just the high-temperature data points

534   ($\geq$240 K) for each residue, and extrapolated to the temperature at which order would be maximized ($1 - S^2 = 0$).

535   To predict global behavior, at each temperature we averaged across all residues the predicted $1 - S^2$ values from

536   the fit, making sure to floor non-physical predicted values of $1 - S^2 < 0$ to 0, as in (Lee and Wand, 2001).

537

559

560   The authors declare that no competing interests exist.

561

562   **References**

563   Alcorn, T., and Juers, D.H. (2010). Progress in rational methods of cryoprotection in macromolecular

564   crystallography. Acta crystallographica Section D, Biological crystallography *66*, 366-373.

565   Baldwin, A.J., and Kay, L.E. (2009). NMR spectroscopy brings invisible protein states into focus. Nature

566   chemical biology *5*, 808-814.

567   Burnley, B.T., Afonine, P.V., Adams, P.D., and Gros, P. (2012). Modelling dynamics in protein crystal structures

568   by ensemble refinement. eLife *1*, e00311.

569   Butterfoss, G.L., Richardson, J.S., and Hermans, J. (2005). Protein imperfections: separating intrinsic from

570   extrinsic variation of torsion angles. Acta crystallographica Section D, Biological crystallography *61*, 88-98.

571   Chinte, U., Shah, B., Chen, Y.S., Pinkerton, A.A., Schall, C.A., and Hanson, B.L. (2007). Cryogenic (<20 K)

572   helium cooling mitigates radiation damage to protein crystals. Acta crystallographica Section D, Biological

573   crystallography *63*, 486-492.

574   Cohen, A.E., Ellis, P.J., Miller, M.D., Deacon, A.M., and Phizackerley, R.P. (2002). An automated system to

575   mount cryo-cooled protein crystals on a synchrotron beam line, using compact sample cassettes and a small-scale

576   robot. Journal of applied crystallography *35*, 720-726.

577 Cohen, A.E., Soltis, S.M., Gonzalez, A., Aguila, L., Alonso-Mori, R., Barnes, C.O., Baxter, E.L., Brehmer, W.,
578 Brewster, A.S., Brunger, A.T.*, et al.* (2014). Goniometer-based femtosecond crystallography with X-ray free
579 electron lasers. Proceedings of the National Academy of Sciences of the United States of America *111*, 17122-
580 17127.

581 Davis, I.W., Arendall, W.B., 3rd, Richardson, D.C., and Richardson, J.S. (2006). The backrub motion: how
582 protein backbone shrugs when a sidechain dances. Structure *14*, 265-274.

583 Deis, L.N., Pemble, C.W.t., Qi, Y., Hagarman, A., Richardson, D.C., Richardson, J.S., and Oas, T.G. (2014).
584 Multiscale conformational heterogeneity in staphylococcal protein a: possible determinant of functional plasticity.
585 Structure *22*, 1467-1477.

586 Doster, W. (2010). The protein-solvent glass transition. Biochim Biophys Acta *1804*, 3-14.

587 Dror, R.O., Dirks, R.M., Grossman, J.P., Xu, H., and Shaw, D.E. (2012). Biomolecular simulation: a
588 computational microscope for molecular biology. Annual review of biophysics *41*, 429-452.

589 Eisenmesser, E.Z., Bosco, D.A., Akke, M., and Kern, D. (2002). Enzyme dynamics during catalysis. Science *295*,
590 1520-1523.

591 Eisenmesser, E.Z., Millet, O., Labeikovsky, W., Korzhnev, D.M., Wolf-Watz, M., Bosco, D.A., Skalicky, J.J.,
592 Kay, L.E., and Kern, D. (2005). Intrinsic dynamics of an enzyme underlies catalysis. Nature *438*, 117-121.

593 Emsley, P., Lohkamp, B., Scott, W.G., and Cowtan, K. (2010). Features and development of Coot. Acta
594 crystallographica Section D, Biological crystallography *66*, 486-501.

595 Fenwick, R.B., van den Bedem, H., Fraser, J.S., and Wright, P.E. (2014). Integrated description of protein
596 dynamics from room-temperature X-ray crystallography and NMR. Proceedings of the National Academy of
597 Sciences of the United States of America *111*, E445-454.

598 Fraser, J.S., Clarkson, M.W., Degnan, S.C., Erion, R., Kern, D., and Alber, T. (2009). Hidden alternative
599 structures of proline isomerase essential for catalysis. Nature *462*, 669-673.

600 Fraser, J.S., van den Bedem, H., Samelson, A.J., Lang, P.T., Holton, J.M., Echols, N., and Alber, T. (2011).
601 Accessing protein conformational ensembles using room-temperature X-ray crystallography. Proceedings of the
602 National Academy of Sciences of the United States of America *108*, 16247-16252.

603 Frauenfelder, H., Hartmann, H., Karplus, M., Kuntz, I.D., Jr., Kuriyan, J., Parak, F., Petsko, G.A., Ringe, D.,
604 Tilton, R.F., Jr., Connolly, M.L.*, et al.* (1987). Thermal expansion of a protein. Biochemistry *26*, 254-261.

605 Frauenfelder, H., Petsko, G.A., and Tsernoglou, D. (1979). Temperature-dependent X-ray diffraction as a probe of
606 protein structural dynamics. Nature *280*, 558-563.

607 Frauenfelder, H., Sligar, S.G., and Wolynes, P.G. (1991). The energy landscapes and motions of proteins. Science
608 *254*, 1598-1603.

609 Fukuda, Y., and Inoue, T. (2015). High-temperature and high-resolution crystallography of thermostable copper
610 nitrite reductase. Chemical communications.

611 Garman, E.F. (2010). Radiation damage in macromolecular crystallography: what is it and why should we care?
612 Acta crystallographica Section D, Biological crystallography *66*, 339-351.

613 Halabi, N., Rivoire, O., Leibler, S., and Ranganathan, R. (2009). Protein sectors: evolutionary units of three-
614 dimensional structure. Cell *138*, 774-786.

Halle, B. (2004). Biomolecular cryocrystallography: structural changes during flash-cooling. Proceedings of the National Academy of Sciences of the United States of America *101*, 4793-4798.

Hattne, J., Echols, N., Tran, R., Kern, J., Gildea, R.J., Brewster, A.S., Alonso-Mori, R., Glockner, C., Hellmich, J., Laksmono, H.*, et al.* (2014). Accurate macromolecular structures using minimal measurements from X-ray free-electron lasers. Nature methods *11*, 545-548.

Henzler-Wildman, K., and Kern, D. (2007). Dynamic personalities of proteins. Nature *450*, 964-972.

Hirata, K., Shinzawa-Itoh, K., Yano, N., Takemura, S., Kato, K., Hatanaka, M., Muramoto, K., Kawahara, T., Tsukihara, T., Yamashita, E.*, et al.* (2014). Determination of damage-free crystal structure of an X-ray-sensitive protein using an XFEL. Nature methods *11*, 734-736.

Holton, J.M. (2009). A beginner's guide to radiation damage. Journal of synchrotron radiation *16*, 133-142.

Keedy, D.A., van den Bedem, H., Sivak, D.A., Petsko, G.A., Ringe, D., Wilson, M.A., and Fraser, J.S. (2014). Crystal cryocooling distorts conformational heterogeneity in a model michaelis complex of DHFR. Structure *22*, 899-910.

Kern, J., Tran, R., Alonso-Mori, R., Koroidov, S., Echols, N., Hattne, J., Ibrahim, M., Gul, S., Laksmono, H., Sierra, R.G.*, et al.* (2014). Taking snapshots of photosynthetic water oxidation using femtosecond X-ray diffraction and spectroscopy. Nature communications *5*, 4371.

Lang, P.T., Holton, J.M., Fraser, J.S., and Alber, T. (2014). Protein structural ensembles are revealed by redefining X-ray electron density noise. Proceedings of the National Academy of Sciences of the United States of America *111*, 237-242.

Lang, P.T., Ng, H.L., Fraser, J.S., Corn, J.E., Echols, N., Sales, M., Holton, J.M., and Alber, T. (2010). Automated electron-density sampling reveals widespread conformational polymorphism in proteins. Protein science : a publication of the Protein Society *19*, 1420-1431.

Lee, A.L., and Wand, A.J. (2001). Microscopic origins of entropy, heat capacity and the glass transition in proteins. Nature *411*, 501-504.

Lewandowski, J.R., Halse, M.E., Blackledge, M., and Emsley, L. (2015). Protein dynamics. Direct observation of hierarchical protein dynamics. Science *348*, 578-581.

Motlagh, H.N., Wrabl, J.O., Li, J., and Hilser, V.J. (2014). The ensemble nature of allostery. Nature *508*, 331-339.

Ollikainen, N., Smith, C.A., Fraser, J.S., and Kortemme, T. (2013). Flexible backbone sampling methods to model and design protein alternative conformations. Methods in enzymology *523*, 61-85.

Rejto, P.A., and Freer, S.T. (1996). Protein conformational substates from X-ray crystallography. Progress in biophysics and molecular biology *66*, 167-196.

Ringe, D., and Petsko, G.A. (2003). The 'glass transition' in protein dynamics: what it is, why it occurs, and how to exploit it. Biophysical chemistry *105*, 667-680.

Schiro, G., Fichou, Y., Gallat, F.X., Wood, K., Gabel, F., Moulin, M., Hartlein, M., Heyden, M., Colletier, J.P., Orecchini, A.*, et al.* (2015). Translational diffusion of hydration water correlates with functional motions in folded and intrinsically disordered proteins. Nature communications *6*, 6490.

651   Schlegel, J., Armstrong, G.S., Redzic, J.S., Zhang, F., and Eisenmesser, E.Z. (2009). Characterizing and
652   controlling the inherent dynamics of cyclophilin-A. Protein science : a publication of the Protein Society *18*, 811-
653   824.

654   Schlichting, I. (2015). Structural biology: Photosynthetic complex in close-up. Nature *517*, 26-27.

655   Smith, C.A., Ban, D., Pratihar, S., Giller, K., Schwiegk, C., de Groot, B.L., Becker, S., Griesinger, C., and Lee, D.
656   (2015). Population shuffling of protein conformations. Angew Chem Int Ed Engl *54*, 207-210.

657   Smith, J.L., Hendrickson, W.A., Honzatko, R.B., and Sheriff, S. (1986). Structural heterogeneity in protein
658   crystals. Biochemistry *25*, 5018-5027.

659   Spence, J.C., Weierstall, U., and Chapman, H.N. (2012). X-ray lasers for structural and dynamic biology. Reports
660   on progress in physics Physical Society *75*, 102601.

661   Suga, M., Akita, F., Hirata, K., Ueno, G., Murakami, H., Nakajima, Y., Shimizu, T., Yamashita, K., Yamamoto,
662   M., Ago, H.*, et al.* (2015). Native structure of photosystem II at 1.95 A resolution viewed by femtosecond X-ray
663   pulses. Nature *517*, 99-103.

664   Team, R. (2014). R: A Language and Environment for Statistical Computing (Vienna, Austria: R Foundation for
665   Statistical Computing).

666   Teeter, M.M., Yamano, A., Stec, B., and Mohanty, U. (2001). On the nature of a glassy state of matter in a
667   hydrated protein: Relation to protein function. Proceedings of the National Academy of Sciences of the United
668   States of America *98*, 11242-11247.

669   Tilton, R.F., Jr., Dewan, J.C., and Petsko, G.A. (1992). Effects of temperature on protein structure and dynamics:
670   X-ray crystallographic studies of the protein ribonuclease-A at nine different temperatures from 98 to 320 K.
671   Biochemistry *31*, 2469-2481.

672   Uervirojnangkoorn, M., Zeldin, O.B., Lyubimov, A.Y., Hattne, J., Brewster, A.S., Sauter, N.K., Weis, W.I., and
673   Brunger, A.T. (2015). Enabling X-ray Free Electron Laser Crystallography for Challenging Biological Systems
674   from a Limited Number of Crystals. eLife *In Press*.

675   van den Bedem, H., Bhabha, G., Yang, K., Wright, P.E., and Fraser, J.S. (2013). Automated identification of
676   functional dynamic contact networks from X-ray crystallography. Nature methods *10*, 896-902.

677   van den Bedem, H., Dhanik, A., Latombe, J.C., and Deacon, A.M. (2009). Modeling discrete heterogeneity in X-
678   ray diffraction data by fitting multi-conformers. Acta crystallographica Section D, Biological crystallography *65*,
679   1107-1117.

680   van den Bedem, H., and Fraser, J.S. (2015). Integrative, Dynamic Structural Biology at Atomic Resolution—It's
681   About Time. Nature methods *In Press*.

682   Warkentin, M., Badeau, R., Hopkins, J.B., and Thorne, R.E. (2012). Spatial distribution of radiation damage to
683   crystalline proteins at 25-300 K. Acta crystallographica Section D, Biological crystallography *68*, 1108-1117.

684   Warkentin, M., Hopkins, J.B., Badeau, R., Mulichak, A.M., Keefe, L.J., and Thorne, R.E. (2013). Global
685   radiation damage: temperature dependence, time dependence and how to outrun it. Journal of synchrotron
686   radiation *20*, 7-13.

687   Warkentin, M., and Thorne, R.E. (2009). Slow cooling of protein crystals. Journal of applied crystallography *42*,
688   944-952.

689   Woldeyes, R.A., Sivak, D.A., and Fraser, J.S. (2014). E pluribus unum, no more: from one crystal, many
690   conformations. Current opinion in structural biology *28*, 56-62.

691

692

	100 K	150 K	180 K	240 K	260 K	280 K	300 K	310 K
PDB ID	4YUG	4YUH	4YUI	4YUJ	4YUK	4YUL	4YUM	4YUN
Wavelength	0.9767	0.9767	0.9767	0.9767	0.9767	0.9767	0.9767	0.9767
Resolution range	33.58 - 1.48 (1.53 - 1.48)	16.95 - 1.34 (1.39 - 1.34)	16.12 - 1.38 (1.43 - 1.38)	34.05 - 1.42 (1.47 - 1.42)	33.98 - 1.48 (1.53 - 1.48)	25.23 - 1.42 (1.47 - 1.42)	22.67 - 1.5 (1.55 - 1.50)	22.66 - 1.58 (1.64 - 1.58)
Space group	$P2_12_12_1$	$P2_12_12_1$	$P2_12_12_1$	$P2_12_12_1$	$P2_12_12_1$	$P2_12_12_1$	$P2_12_12_1$	$P2_12_12_1$
Unit cell (a, b, c)	42.24 51.91 88.06	42.45 51.82 88.01	42.42 51.96 88.21	43.04 53.22 88.63	43.09 52.79 88.81	43.00 52.61 89.12	43.01 52.61 89.32	42.85 52.58 89.41
Total reflections	160129 (15842)	160780 (7437)	154202 (11295)	152578 (13600)	134699 (13381)	168932 (15019)	144734 (14433)	125225 (12326)
Unique reflections	32657 (3240)	42288 (3471)	39548 (3820)	38881 (3710)	34411 (3391)	38763 (3794)	32999 (3254)	28291 (2760)
Multiplicity	4.9 (4.9)	3.8 (2.1)	3.9 (3.0)	3.9 (3.7)	3.9 (3.9)	4.4 (4.0)	4.4 (4.4)	4.4 (4.5)
Completeness (%)	99 (100)	95 (80)	97 (95)	99 (96)	100 (100)	100 (100)	99 (100)	100 (100)
Mean I/sigma(I)	14.07 (1.57)	25.95 (3.24)	16.47 (1.64)	12.86 (1.66)	10.09 (1.46)	15.51 (1.52)	16.90 (1.63)	13.26 (1.45)
Wilson B-factor	16.07	13.12	16.95	15.55	16.06	17.62	19.75	21.44
R-merge (%)	6.8 (99.4)	3.0 (29.4)	4.2 (71.8)	6.2 (99.2)	8.1 (104.3)	4.9 (100.0)	4.7 (101.7)	6.7 (127.3)
R-meas (%)	7.6 (111.0)	3.4 (36.9)	4.8 (85.6)	7.2 (116.8)	9.4 (120.8)	5.6 (115.3)	5.4 (115.9)	7.6 (144.5)
CC1/2	1.00 (0.62)	1.00 (0.90)	1.00 (0.60)	1.00 (0.50)	1.00 (0.52)	1.00 (0.52)	1.00 (0.59)	1.00 (0.56)
CC*	1.00 (0.88)	1.00 (0.97)	1.00 (0.87)	1.00 (0.82)	1.00 (0.83)	1.00 (0.83)	1.00 (0.86)	1.00 (0.85)
Refinement resolution range	33.085 - 1.48 (1.558 - 1.48)	19.117 - 1.34 (1.394 - 1.34)	16.995 - 1.38 (1.435 - 1.38)	34.055 - 1.42 (1.477 - 1.42)	33.98 - 1.48 (1.547 - 1.48)	25.23 - 1.42 (1.477 - 1.42)	22.67 - 1.5 (1.579 - 1.5)	25.222 - 1.58 (1.679 - 1.58)
Reflections used in refinement	32627 (4654)	42278 (3932)	39545 (4265)	38879 (4161)	34411 (4237)	38762 (4256)	32999 (4643)	28287 (4632)
Reflection	1028	1325	1238	1218	1080	1217	1036	889

s used for R-free	(147)	(125)	(133)	(130)	(133)	(133)	(145)	(146)
R-work (%)	13.3 (20.4)	12.4 (16.4)	13.3 (25.4)	12.6 (26.3)	13.1 (26.0)	11.1 (22.6)	10.8 (20.0)	11.7 (21.8)
R-free (%)	18.3 (26.8)	15.6 (21.3)	17.5 (33.0)	15.6 (30.4)	16.8 (31.2)	14.3 (25.5)	14.4 (24.8)	15.0 (28.8)
Number of non-hydrogen atoms	2279	2433	1969	1993	2035	2120	2096	2172
Macromolecule atoms	1933	2132	1745	1750	1837	1924	1952	2061
Protein residues	165	164	164	163	163	163	163	163
RMS(bonds)	0.009	0.008	0.008	0.009	0.009	0.008	0.009	0.009
RMS(angles)	1.16	1.20	1.23	1.20	1.16	1.16	1.14	1.14
Ramachandran favored (%)	97	94	97	96	97	96	97	96
Ramachandran allowed (%)	3.3	5.7	2.7	4.1	3	4.2	3.3	3.9
Ramachandran outliers (%)	0	0	0	0	0	0	0	0
Rotamer outliers (%)	2.4	1.3	0.53	1.1	1.5	1.9	1.4	0.88
Clashscore	0.57	1.08	0.00	1.24	0.27	0.78	0.52	0.00
Average B-factor	21.74	17.25	21.85	20.14	20.00	21.48	24.09	25.77
Macromolecule Average B-factor	18.48	14.67	19.99	17.95	18.17	19.61	22.82	24.94
Solvent Average B-factor	39.99	35.54	36.34	35.89	37.01	39.89	41.23	41.30

694   **Table 1:** Crystallographic statistics for multitemperature synchrotron datasets collected on a single crystal per
695   dataset. Statistics for the highest-resolution shell are shown in parentheses.
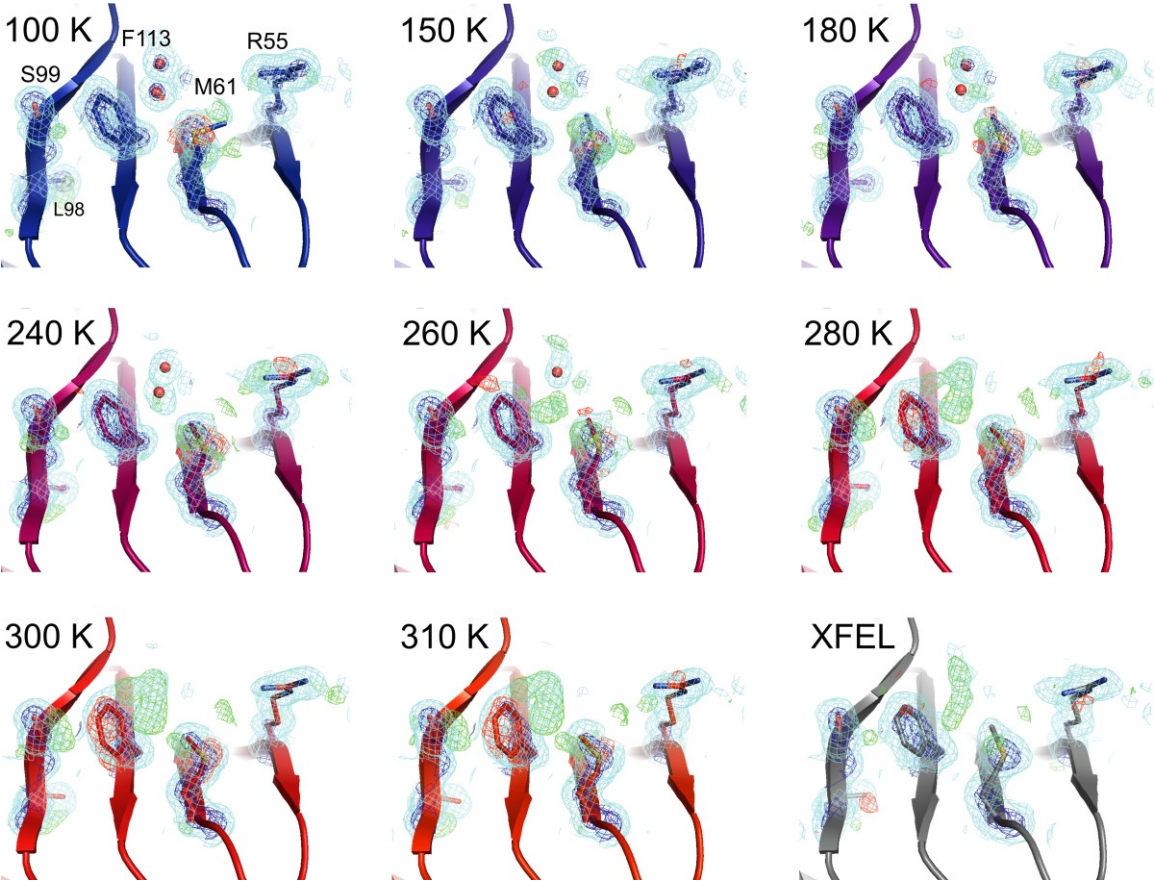
Table 1 - Figure Supplement 1: Single-conformer models cannot explain the crystallographic data at higher temperatures. The CypA dynamic network is shown after molecular replacement and refinement (including automated water placement) in PHENIX, before any manual rebuilding. The major state is well supported by 2mFo-DFc electron density contoured at 0.6 σ (cyan mesh) and 3.0 σ (dark blue mesh) for all datasets, but mFo-DFc difference electron density becomes more negative for the major state (-3.0 σ, red mesh) and more positive for the unmodeled minor state (+3.0 σ, green mesh) as temperature increases across the synchrotron datasets (blue to red), especially at and above 240 K. Full-occupancy water molecules (red spheres) are automatically placed by PHENIX near the Phe113 minor state in lower-temperature, but not in higher-temperature synchrotron models because they are mutually exclusive with the secondary Phe113 conformation.

710
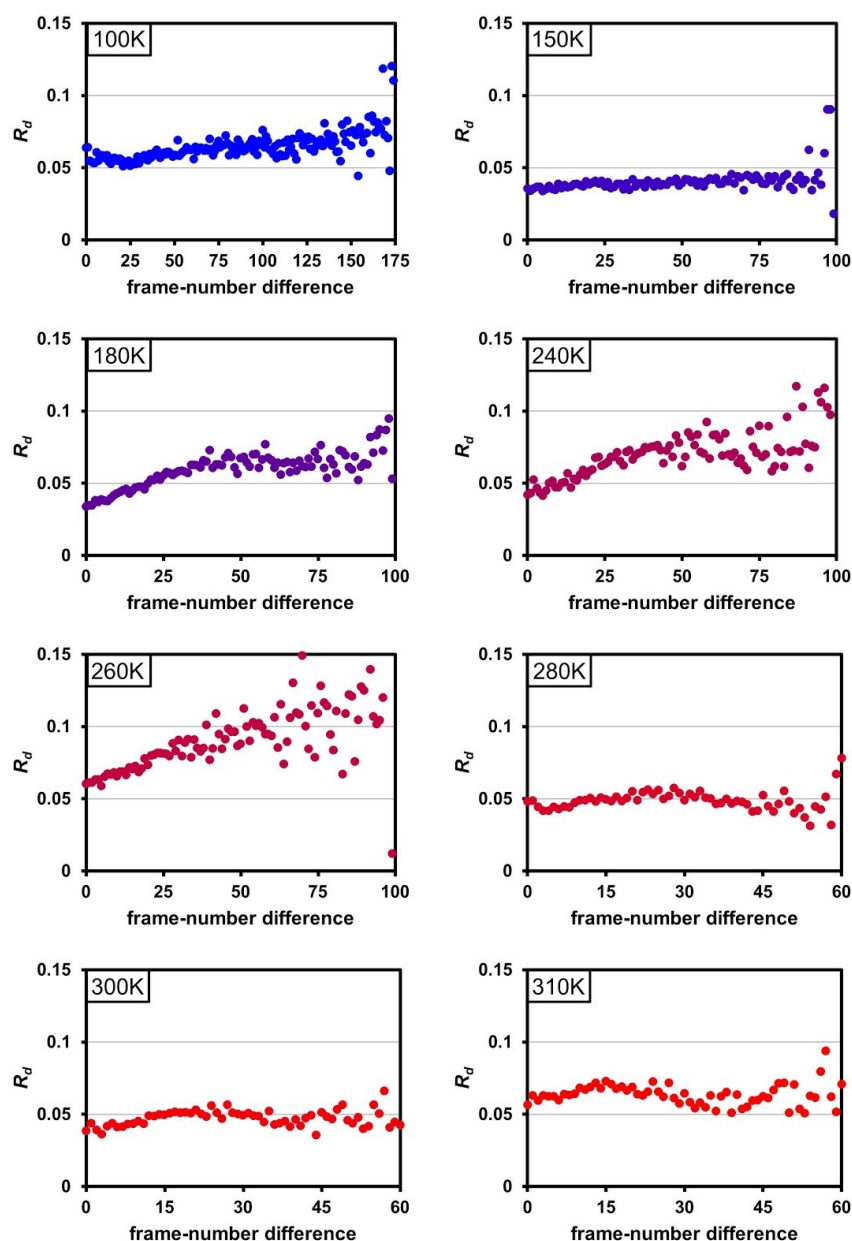
Table 1 - Figure Supplement 2: Radiation damage is minimal across data collection temperatures. Plots of R_d vs. frame-number difference for each dataset in the multitemperature trajectory reveal only minimal radiation damage. The datasets around 180-260 K exhibit higher R_d in later frames, which may reflect either a time-dependent cryocooling artifact or radiation damage at these intermediate temperatures. Although the rate of X-ray damage varies strongly with temperature, the data collection strategy was adjusted to yield a comparable amount of damage per frame. Therefore, there is no correlation between data collection temperature and the overall extent of radiation damage; the highest temperature data sets are equally undamaged as the lowest temperature data sets. By contrast, we observe a strong correlation between data collection temperature and conformational heterogeneity.

720

721

722
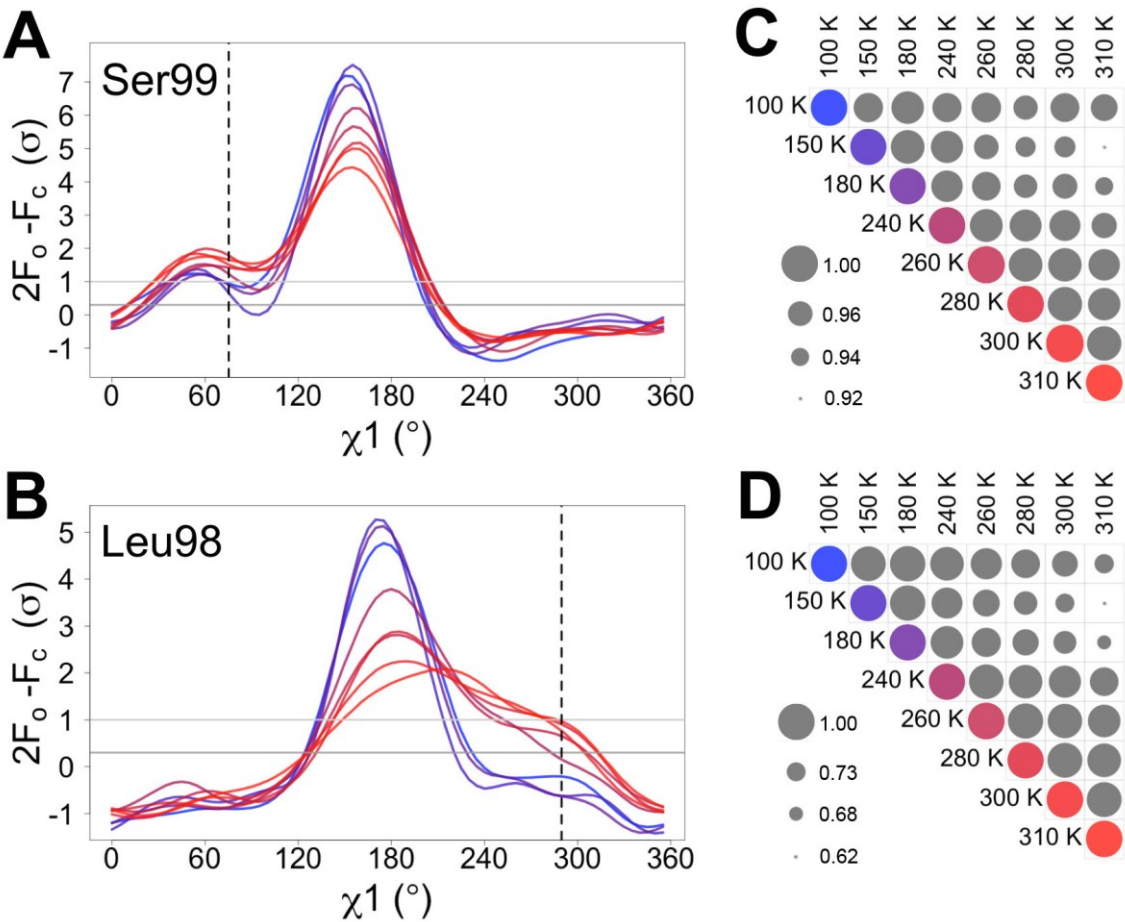
Figure 1: Automated electron density sampling reveals increased conformational redistribution. Ringer curves of 2mFo-DFc electron density vs. χ1 dihedral angle for **(A)** Ser99 and **(B)** Leu98 show large peaks for modeled major conformations, and also smaller peaks for additional minor conformations (dashed vertical lines). These secondary peaks become more evident as temperature increases (color gradient from blue to purple to red). A backrub motion was used for Ser99. For **(C)** Ser99 and **(D)** Leu98, a Pearson correlation coefficient was calculated between each pair of Ringer curves from the corresponding panel in **(A)** and **(B)**. Circles in diagonal elements are colored as in **(A)** and **(B)**; circles in off-diagonal elements are all gray but scaled by pairwise correlation coefficient (see legend). Pairs of curves from similar temperatures are generally more correlated to each other (larger circles) than are pairs of curves from more different temperatures (smaller circles).

733

734

735

		RT sync	XFEL	100 K	150 K	180 K	240 K	260 K	280 K	300 K	310 K
R_{free} (%)	*raw qFit*	16.7	25.2	19.0	16.9	18.5	17.5	17.9	15.7	16.3	16.1
	final	14.6	24.9	18.3	15.6	17.5	15.6	16.8	14.3	14.4	15.0
	Δ	-2.1	-0.3	-0.7	-1.3	-1.0	-1.9	-1.1	-1.4	-1.9	-1.1
Molprobity score	*raw qFit*	1.47	1.80	1.79	1.31	1.21	1.18	1.45	1.28	0.95	1.19
	final	1.08	1.39	1.19	1.29	0.63	1.14	0.91	1.25	0.99	0.76
	Δ	-0.39	-0.41	-0.80	-0.02	-0.58	-0.04	-0.54	-0.03	+0.04	-0.43

736 **Table 2:** Improvements in validation statistics from finalizing raw qFit models. Statistics calculated with
737 *phenix.molprobity*.

738
739

740

741
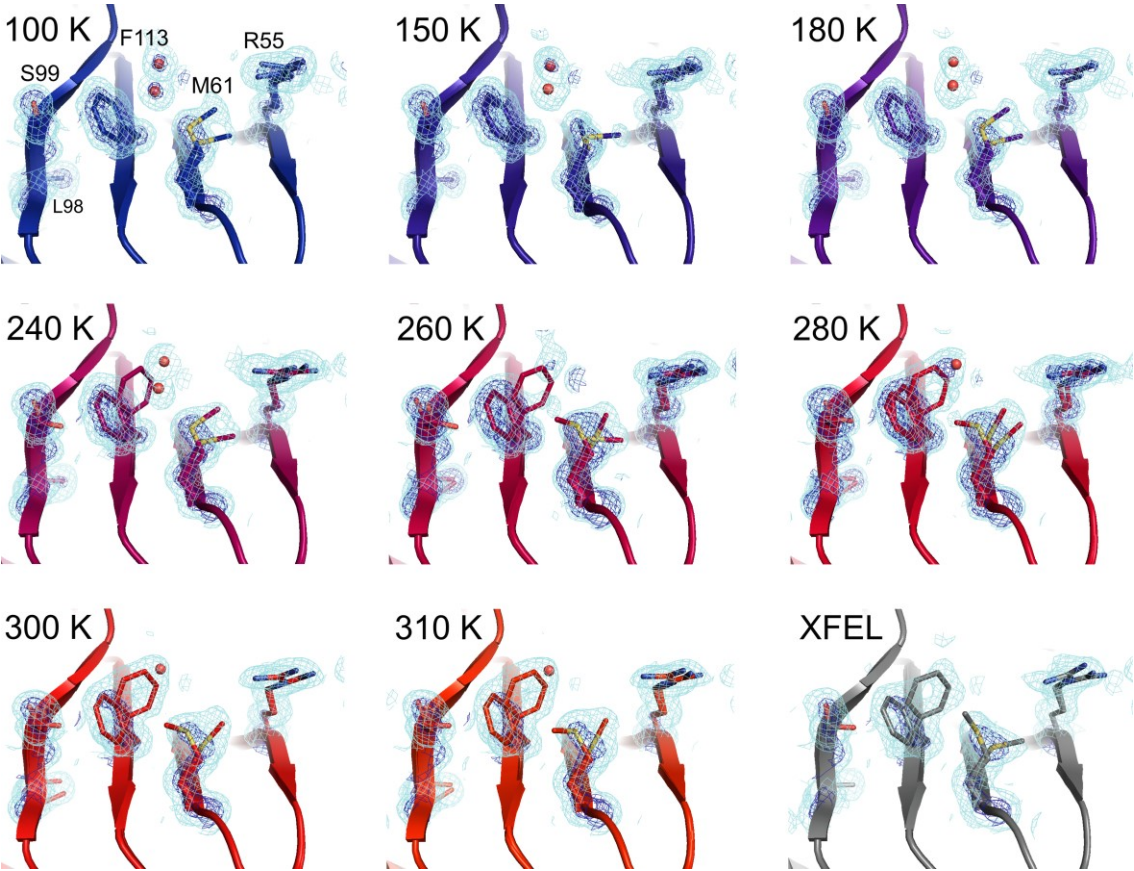
742 **Figure 2: Multiconformer modeling across temperatures captures increasing conformational**
743 **heterogeneity.** Residues extending from the core to the active site of CypA adopt a single conformer at low
744 temperatures, but gradually transition to increasing occupancy of secondary conformations as temperature
745 increases. These conformations are well supported by 2mFo-DFc electron density contoured at 0.6 σ (cyan
746 mesh) and 3.0 σ (dark blue mesh). This is corroborated by the room-temperature XFEL model (gray), which is
747 free from conventional radiation damage and features the same secondary conformations. Water molecules (red
748 spheres) are more fully ordered at low temperatures, but become only partially occupied at higher temperatures
749 because they are mutually exclusive with the secondary Phe113 conformation.
750

751

752
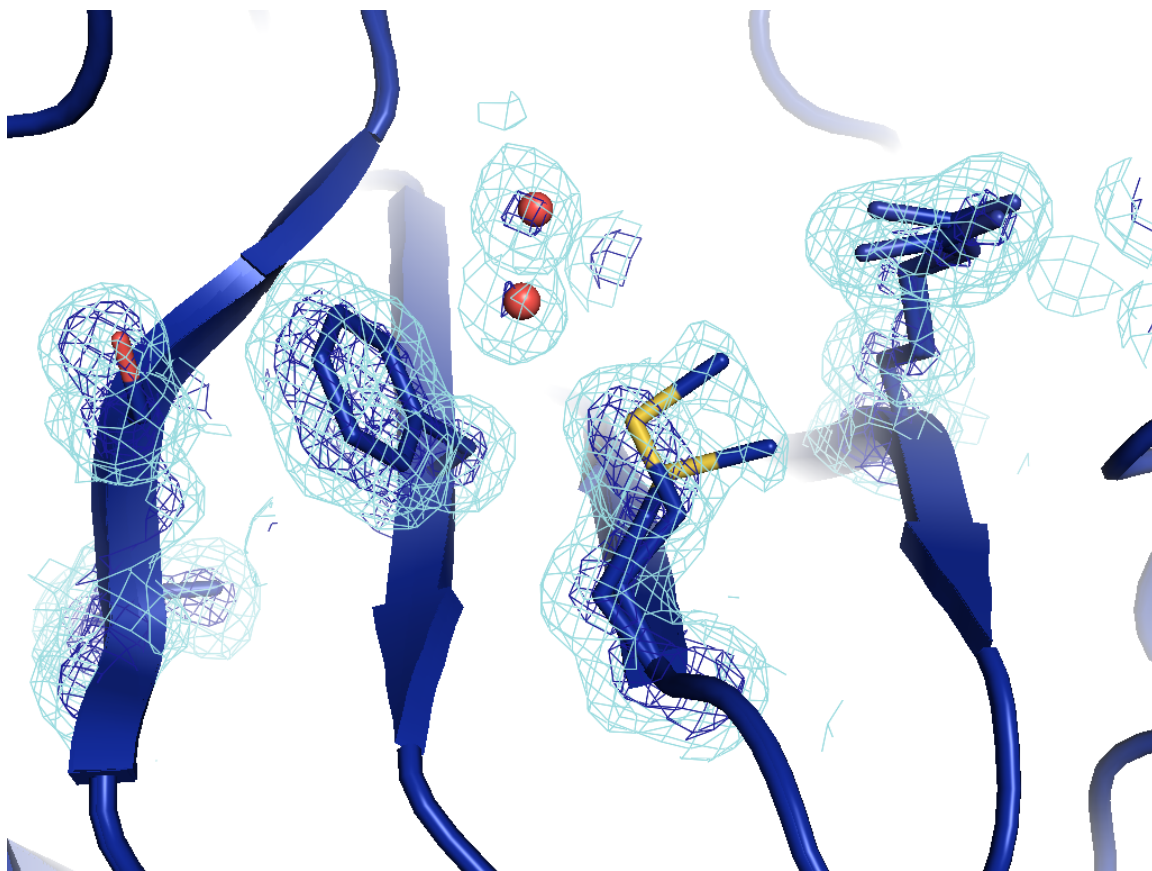
Movie 1: Animated interpolation between electron density maps in temperature trajectory. For each pair of adjacent temperatures (e.g. 100 and 150 K), the temperature regime between them was bisected and an average 2mFo-DFc electron density maps was calculated in reciprocal space using CCP4 utilities, until temperature points were spaced by <1 K. A new multiconformer model is shown when the animation reaches the corresponding temperature.

758

759

760

	XFEL
PDB ID	4YUP
Resolution range	43.98 - 1.75 (1.81 - 1.75)
Space group	$P2_12_12_1$
Unit cell (a, b, c)	42.42 51.82 87.96
Unique reflections	19942 (1894)
Completeness (%)	99 (96)
Wilson B-factor	21.12
Refinement resolution range	43.98 - 1.75 (1.93 - 1.75)
Reflections used in refinement	19936 (4811)
Reflections used for R-free	625 (151)
R-work (%)	20.0 (34.3)
R-free (%)	24.9 (36.1)
Number of non-hydrogen atoms	1762
Macromolecular atomcs	1559
Protein residues	164
RMS(bonds)	0.017
RMS(angles)	1.44
Ramachandran favored (%)	96
Ramachandran allowed (%)	3.6
Ramachandran outliers (%)	0
Rotamer outliers (%)	1.8
Clashscore	1.92
Average B-factor	29.03
macromolecules	26.52
solvent	48.25
Number of TLS groups	3

761 **Table 3:** Crystallographic statistics for room-temperature XFEL dataset collected across 71 crystals. Statistics for
762 the highest-resolution shell are shown in parentheses.

763

	1.2 Å synchrotron
PDB ID	4YUO
Wavelength	0.9795
Resolution range	44.60 - 1.20 (1.24 - 1.20)
Space group	P 21 21 21
Unit cell	42.9 52.43 89.11 90 90 90
Total reflections	307722 (18999)
Unique reflections	58118 (5122)
Multiplicity	5.3 (3.7)
Completeness (%)	91 (82)
Mean I/sigma(I)	10.99 (5.93)
Wilson B-factor	15.22
R-merge (%)	11.2 (20.4)
R-meas (%)	12.2 (23.4)
CC1/2	0.99 (0.96)
CC*	1.00 (0.99)
Refinement resolution range	45.19 - 1.20 (1.23 - 1.20)
Reflections used in refinement	58108 (3657)
Reflections used for R-free	2000 (126)
R-work (%)	12.7 (31.3)
R-free (%)	14.6 (33.5)
Number of non-hydrogen atoms	2327
Macromolecular atoms	2143
Protein residues	163
RMS(bonds)	0.009
RMS(angles)	1.16
Ramachandran favored (%)	96
Ramachandran allowed (%)	4.1
Ramachandran outliers (%)	0
Rotamer outliers (%)	0.84
Clashscore	0.98
Average B-factor	19.62
macromolecules	18.40
solvent	33.86

764 **Table 4:** Crystallographic statistics for room-temperature synchrotron dataset collected on a single crystal.
765 Statistics for the highest-resolution shell are shown in parentheses.

766

767

768
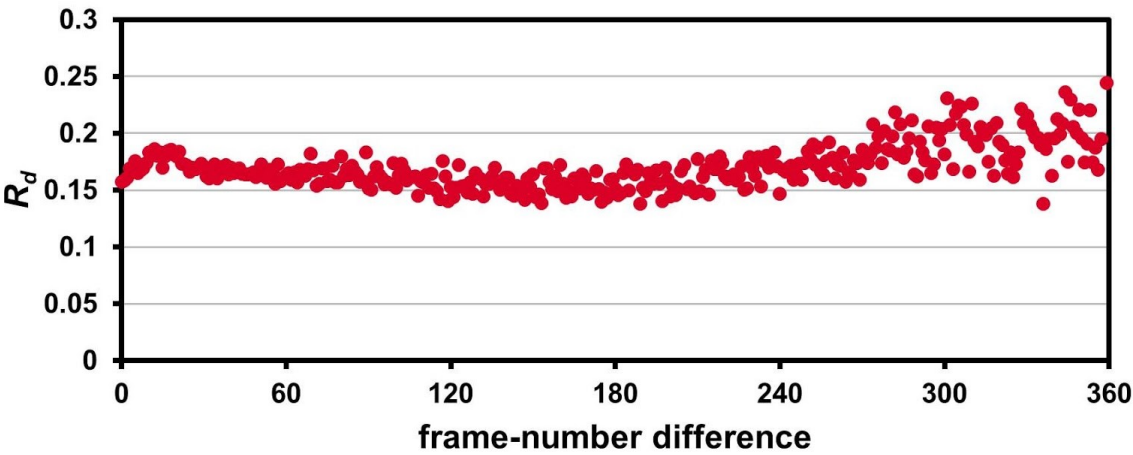
Table 4 - Figure Supplement 1: The 1.2 Å room-temperature CypA synchrotron data shows no signs of radiation damage. A plot of "decay R-factor" (R_d) as a function of frame-number difference (as in **Table 1 - Figure Supplement 2**) has a slope of zero, indicating the absence of radiation damage. R_d is calculated using pairwise observations of unique reflections (*hkl*) with centroids on frames *i* and *j*, and the frame-number difference is given by |*i-j*|. The calculations were performed using a 2.0 Å resolution cutoff.

774

775
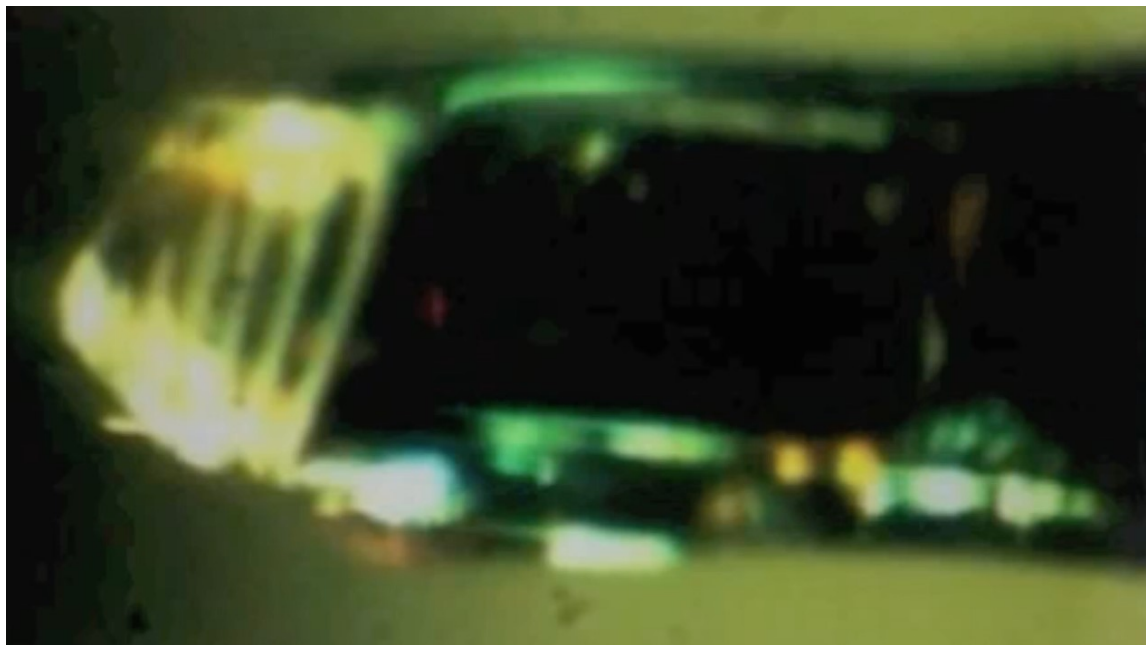
Movie 2: Fixed-target XFEL data collection from CypA crystals at the LCLS XPP end station. Screen capture image of the Blu-Ice GUI showing a video display of a CypA crystal. After each shot, a new damage line appears and the crystal is translated.

779

780
781
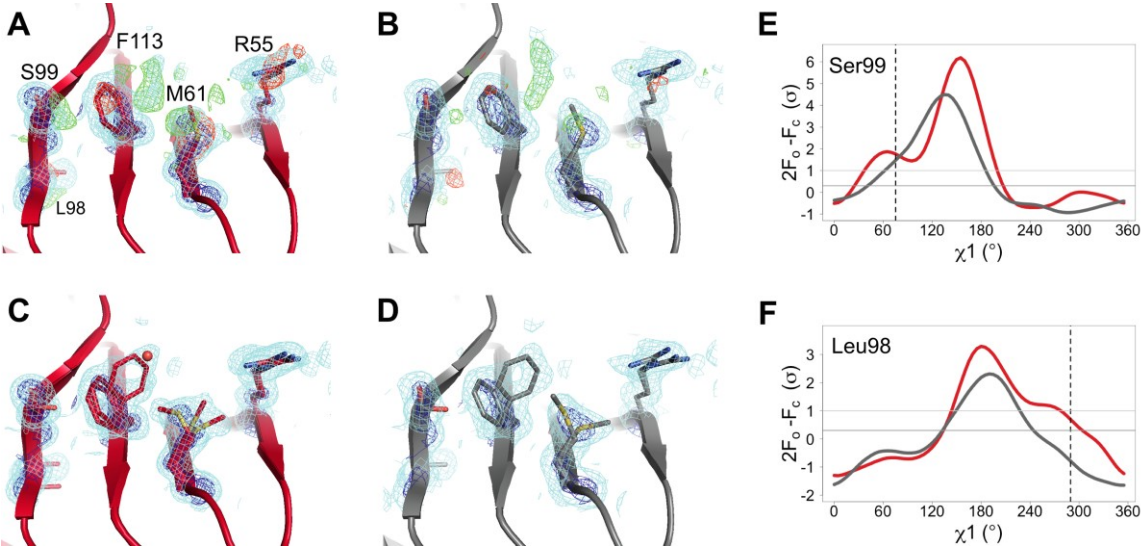
Figure 3: The active-site conformational ensemble of CypA determined without radiation damage at room temperature. (A) Electron density maps for room-temperature synchrotron (red) and (**B**) XFEL (silver) single-conformer models reveal conformational heterogeneity extending from the protein core (Leu98 and Ser99) to the active site (Arg55) of CypA. The primary conformation is well supported by 2mFo-DFc electron density contoured at 0.6 σ (cyan mesh) and 3.0 σ (dark blue mesh). mFo-DFc difference electron density contoured at 3.0 σ (green mesh) and -3.0 σ (red mesh) suggests unmodeled alternative conformations. **(C,D)** Finalized multiconformer models explicitly model these alternative conformations, which are well-supported by 2mFo-DFc electron density. **(E,F)** Ringer electron-density sampling for the single-conformer models shows peaks representing alternative conformations for **(E)** Ser99 and **(F)** Leu98. The primary conformations of both residues are obvious as peaks for both models, but the minor conformations (dashed vertical line; as modeled in 3k0n) are also evident, with 2mFo-DFc values well above the 0.3 σ (darker gray horizontal line) threshold, except for the Leu98 in the XFEL model (due to the lower resolution). A backrub motion of -10˚ positions the backbone properly for Ringer to best detect the minor conformation for Ser99, but not for Leu98.

798
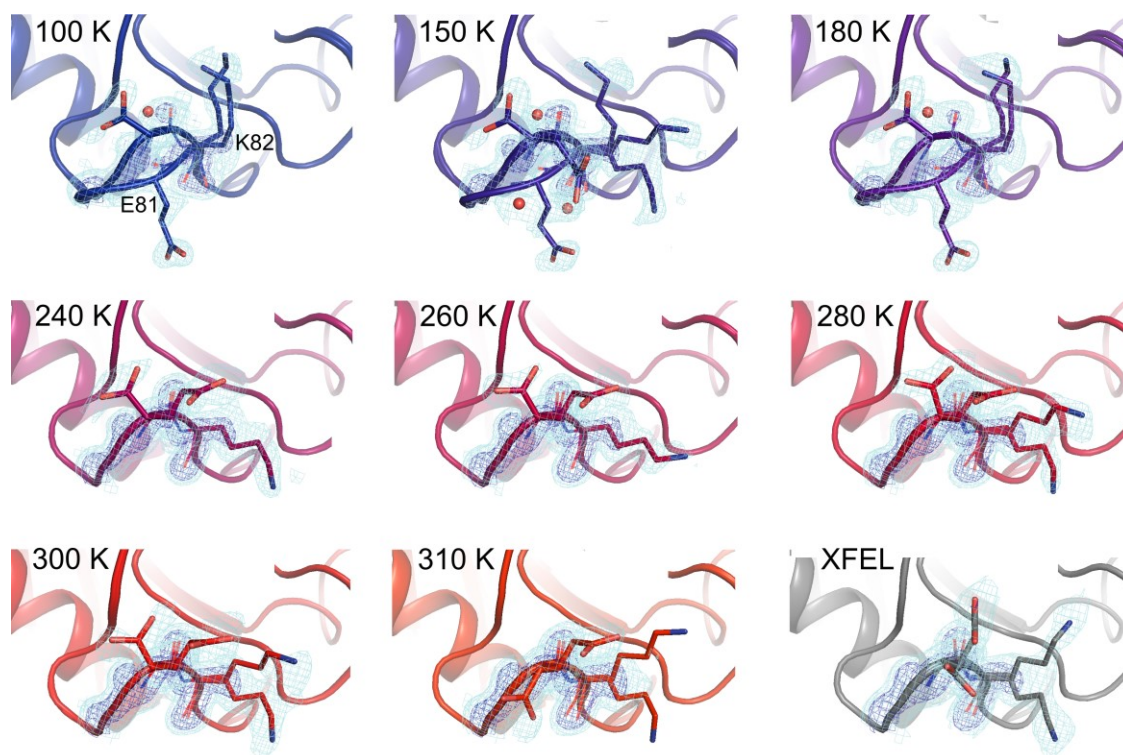
799 **Figure 4: Alternative loop conformations can appear at lower temperatures.** The surface loop containing
800 residues 79-83 adopts alternative conformations at low temperatures (top row) but not at high temperatures
801 (bottom two rows). The secondary loop conformation is separated from the body of the protein by an ordered
802 water molecule (red sphere); the van der Waals interactions between the loop and the water may reflect an
803 enthalpic stabilization that is more dominant at low temperatures. The electron density peak to the right of the
804 water corresponds to the backbone carbonyl oxygen of Glu81. 2mFo-DFc electron density contoured at 0.6 σ
805 (cyan mesh) and 2.0 σ (dark blue mesh).
806

807
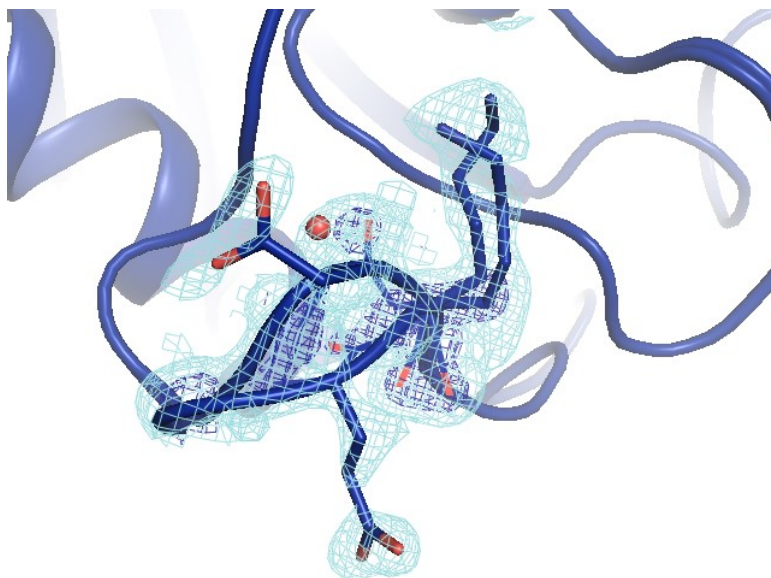
808   **Movie 3:** Animated rotation around the 100 K (blue) and 310 K (red) models and electron density maps from
809   **Figure 4**.

810

811

812

813
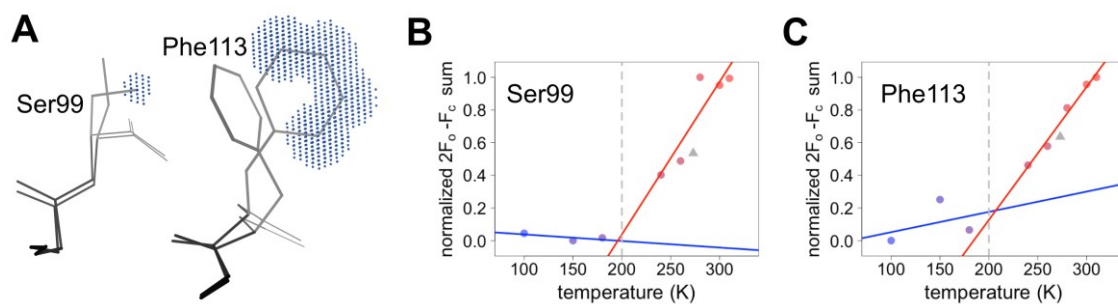
Figure 5: Quantifying temperature titration of conformational heterogeneity in multiconformer models. (A) 2mFo-DFc electron density was summed over the volume occupied by the minor conformation but not the major conformation (blue grid points) for Ser99 and Phe113. **(B,C)** Minor-state 2mFo-DFc electron density increases with temperature. Electron density sums were normalized for each residue. Multitemperature points from synchrotron data are shown in colors corresponding to temperature. The XFEL point is shown as a gray triangle. Best-fit lines are shown for 180 K and below (blue) vs. 240 K and above (red).

820

821
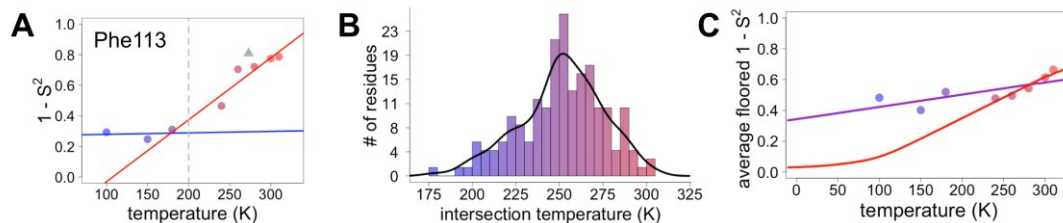
Figure 6: Diversity in temperature dependences of sidechain disorder across CypA does not predict the observed average arrest of disorder. (A) The complement of B-factor-influenced sidechain order parameter for the bond most closely associated with the χ1 dihedral angle for Phe113. Lines reflect least-squares fits to synchrotron models at 180 K and below (blue) vs. 240 K and above (red). Multitemperature synchrotron points in colors; XFEL point (not included in fits) as gray triangle. **(B)** Distribution of the intersection temperature between the <200 and >200 K lines fitted with kernel density function. The peak is near 250 K, although there is a tail toward lower temperatures. Intersection temperatures were <170 K for 4 residues and >330 K for 5 residues. **(C)** Predicted and observed values for the complement of sidechain order parameter, averaged over all residues in CypA. The predicted values were obtained by extrapolating each residue's fit line for 240 K and above (red curve) or for the full 100-300 K (purple curve), flooring the result to 0, then averaging across all residues in CypA. Observed values, similarly floored and averaged, are shown as points.

834
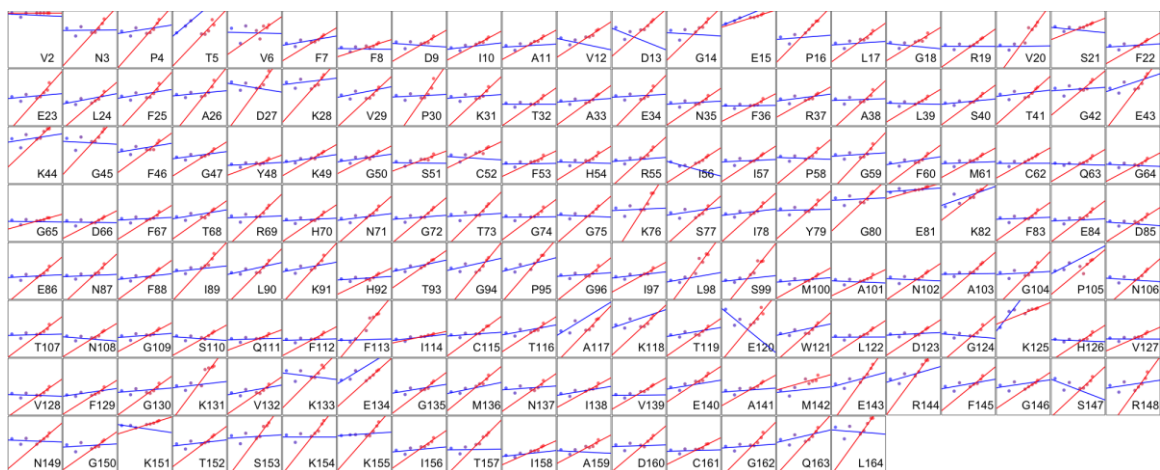
Figure 6 - Figure Supplement 1: Heterogeneous response of sidechain disorder to temperature. The complement of B-factor-influenced sidechain order parameter for the bond most closely associated with the χ1 dihedral angle for all residues in CypA. Lines reflect least-squares fits to synchrotron models for 180 K and below (blue) vs. 240 K and above (red).

839

840

841

842
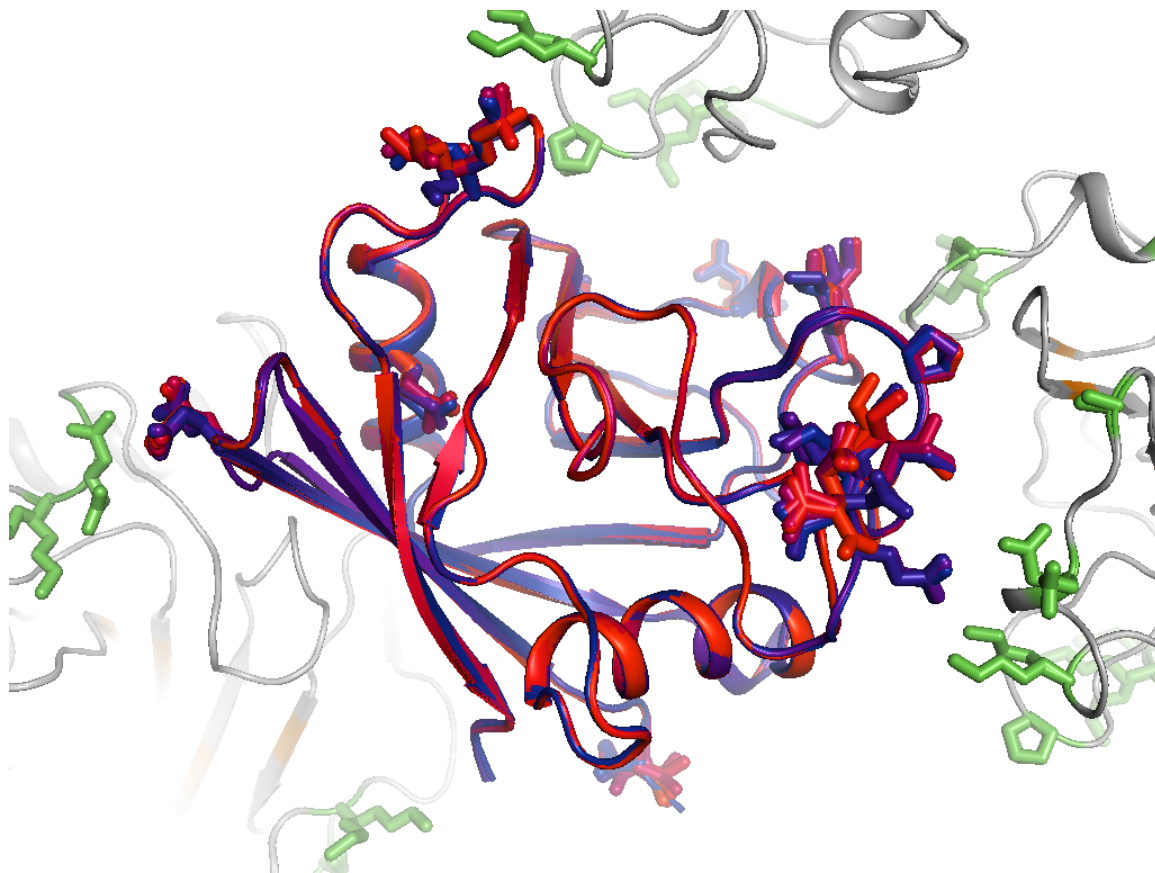
Figure 6 - Figure Supplement 2: Residues with persistent disorder across temperatures are inter-connected in the crystal lattice. Several residues with high $1 - S^2$ values (Val2, Glu15, Gly80, Glu81, Lys82, Pro105, Ala117, Glu120, Lys125, Met142, Ser147, and Lys151) are shown for the central molecule (blue-to-red sticks and backbone) and also in symmetry mates (green sticks, gray backbone). Many of these residues appear to interact with each other via lattice contacts. Frustration in these interactions may lead to persistent disorder.

848

849
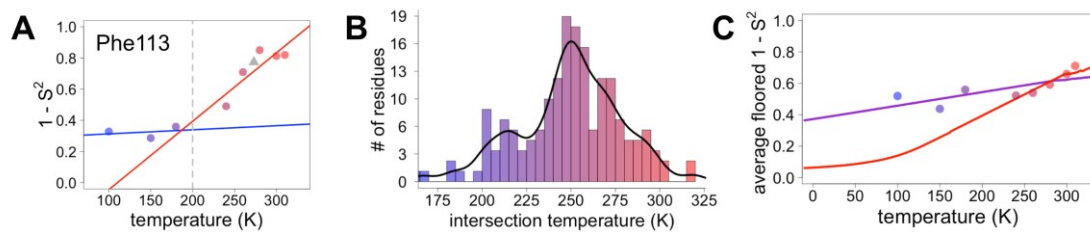
Figure 6 - Figure Supplement 3: Diversity in temperature dependences of sidechain-end disorder across CypA does not predict the observed average arrest of disorder. Each panel is as in **Figure 6**, but the order parameter now models the final heavy-atom to heavy-atom bond for each sidechain (see Methods).
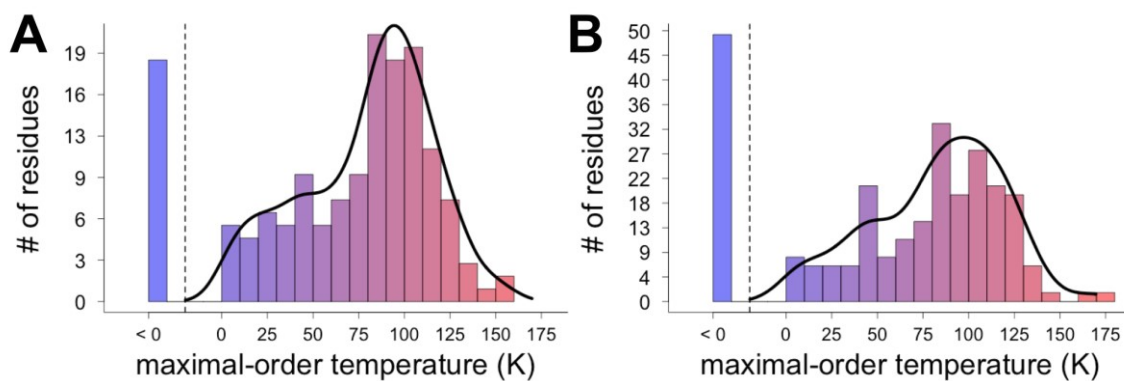
853
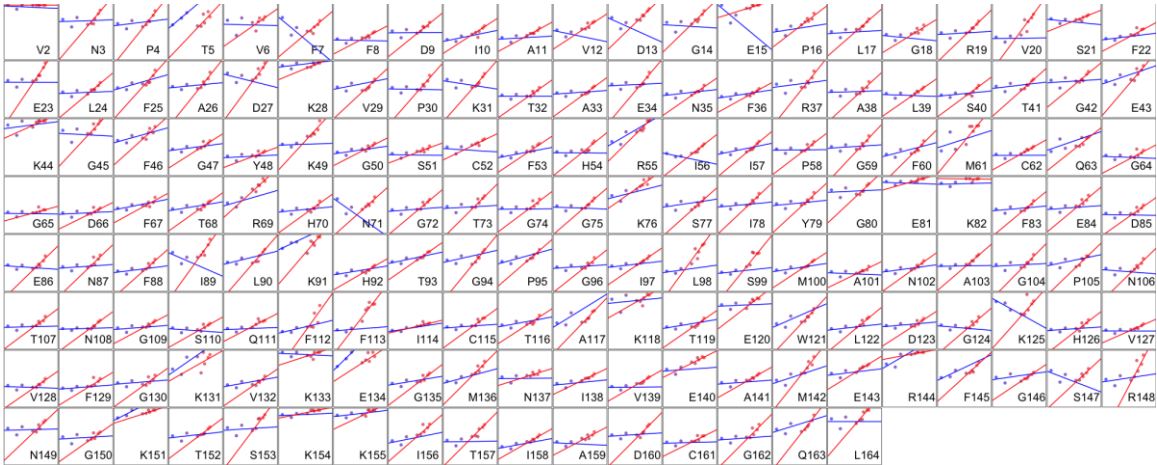
854
Figure 6 -
855 **Figure Supplement 4: Heterogeneous response of sidechain-end disorder to temperature.** The small
856 multiple plots are as in **Figure 6 - Figure Supplement 1**, but the order parameter now models the final heavy-
857 atom to heavy-atom bond for each sidechain (see Methods).

858

859

Figure 6 - Figure Supplement 5: Different residues extrapolate to different maximal-order temperatures.
Fit lines for temperature points at 240 K and above were used to extrapolate to the maximal-order temperature,
at which $1 - S^2 = 0$. **(A)** Order parameter modeling the bond most closely associated with the $\chi 1$ dihedral angle.
(B) Order parameter modeling the final heavy-atom to heavy-atom bond for each sidechain.
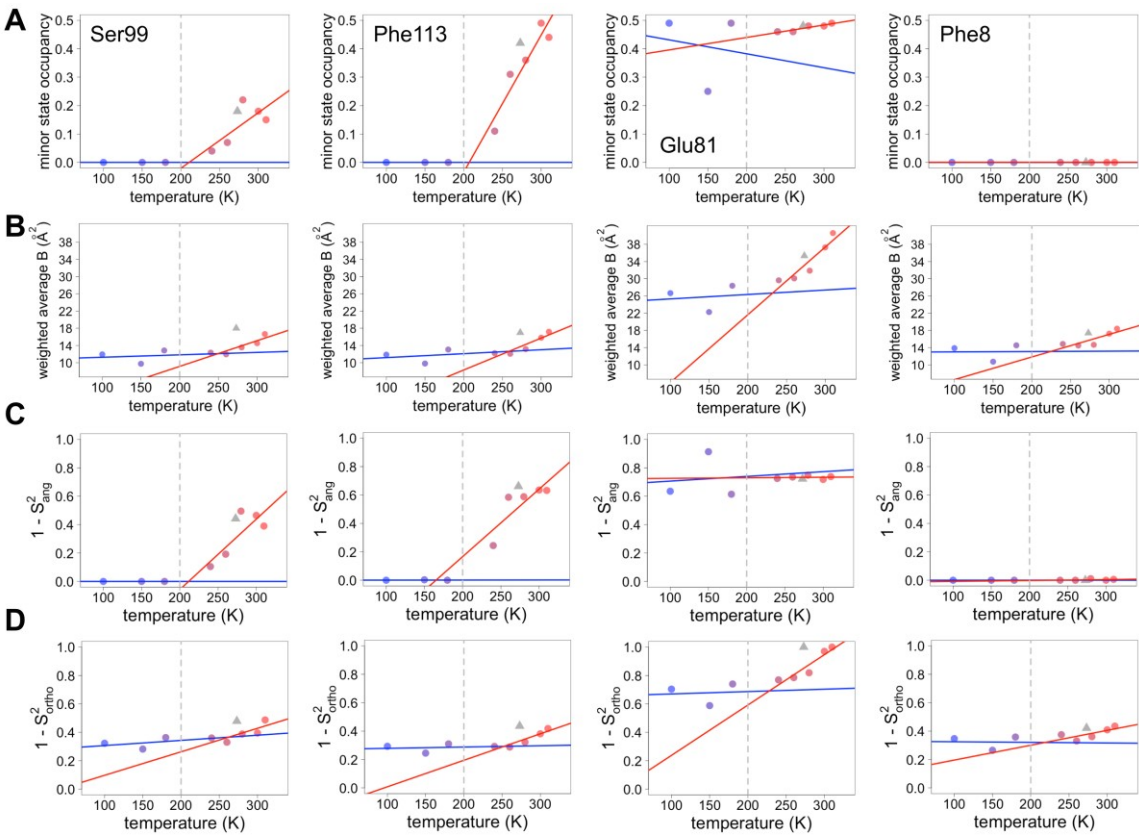
864

Figure 6 - Figure Supplement 6: Both harmonic and non-harmonic flexibility contribute to changes in order parameters with temperature. (A-D) Contributions to χ1 order parameter vs. temperature for four representative residues in CypA. Ser99 and Phe113 are in the active-site network, Glu81 is surface-exposed and adopts alternative conformations at all temperatures (**Figure 4**), and Phe8 is buried in the protein core and is single-rotamer at all temperatures. Similar conformations within the same rotameric well were grouped together for this analysis. **(A)** Occupancy of minor alternative conformations. **(B)** Intra-residue heavy-atom-average B-factor. **(C)** Complement of the S^2_{ang} component of the χ1 order parameter, which uses occupancy-weighted angles between bond vectors across alternative conformations. **(D)** Complement of the S^2_{ortho} component of the χ1 order parameter, which uses occupancy-weighted B-factors. Placement of XFEL points and coloring as in **Figure 6A**.

878
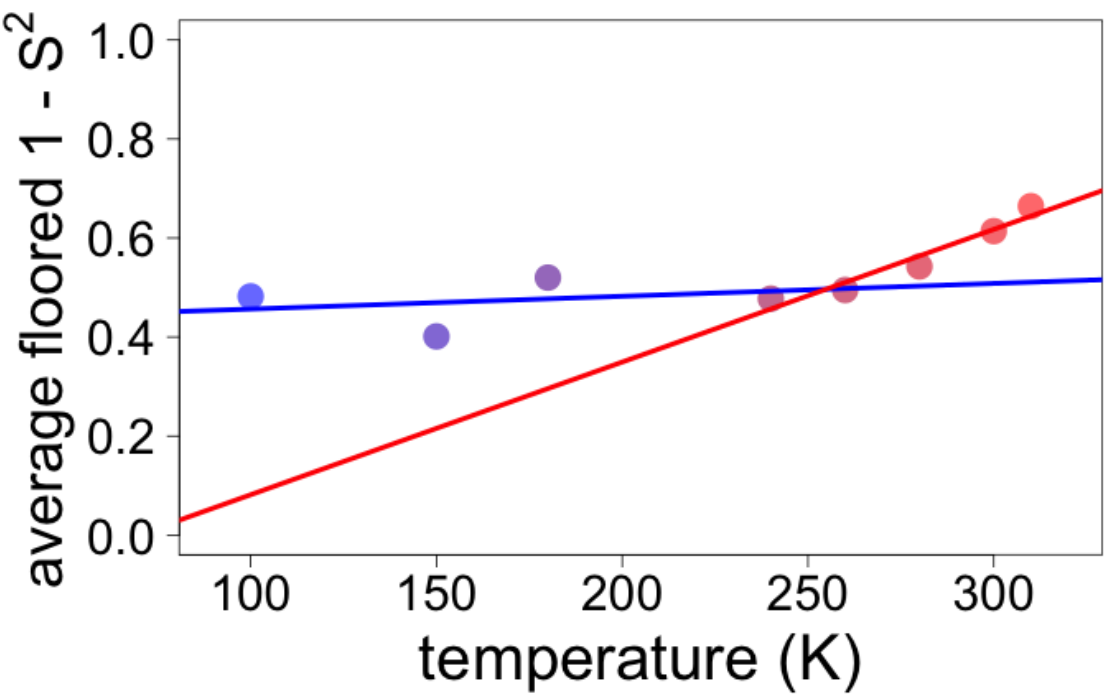
879

880 **Figure 6 - Figure Supplement 7: Globally averaged disorder exhibits an apparent transition near 250 K.**
881 Points indicate observed values for the complement of sidechain order parameters, floored at 0 and then
882 averaged over all residues in CypA, as in **Figure 6**. The blue and red lines represent fits to the $\leq$180 K and $\geq$240
883 K floored and averaged points, respectively. The fits to these globally averaged data suggest a transition at
884 ~250 K, even though the underlying heterogeneity of the individual residue responses does not indicate there is
885 a transition near this temperature.

886

887

888

889

890
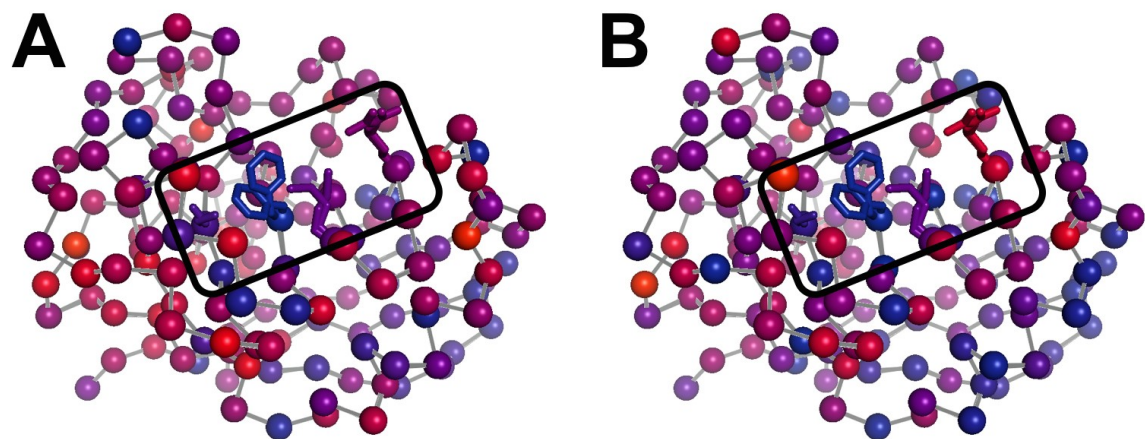
Figure 7: The temperature dependence of sidechain disorder is is nonhomogenously spatially distributed in CypA. Intersection temperatures from **(A)** χ1 order parameters as in **Figure 6B** or **(B)** sidechain terminus order parameters as in **Figure 6 – Figure Supplement 3 B** are mapped to the 1.2 Å room-temperature synchrotron model. Each residue is marked with a sphere colored based on its apparent transition temperature, from low (blue) to high (red). The active-site network is subdivided: Ser99 and Phe113 (left of boxed region) both transition at a low temperature regardless of order parameter bond vector, but Met61 and Arg55 transition at higher, different temperatures.

898

899
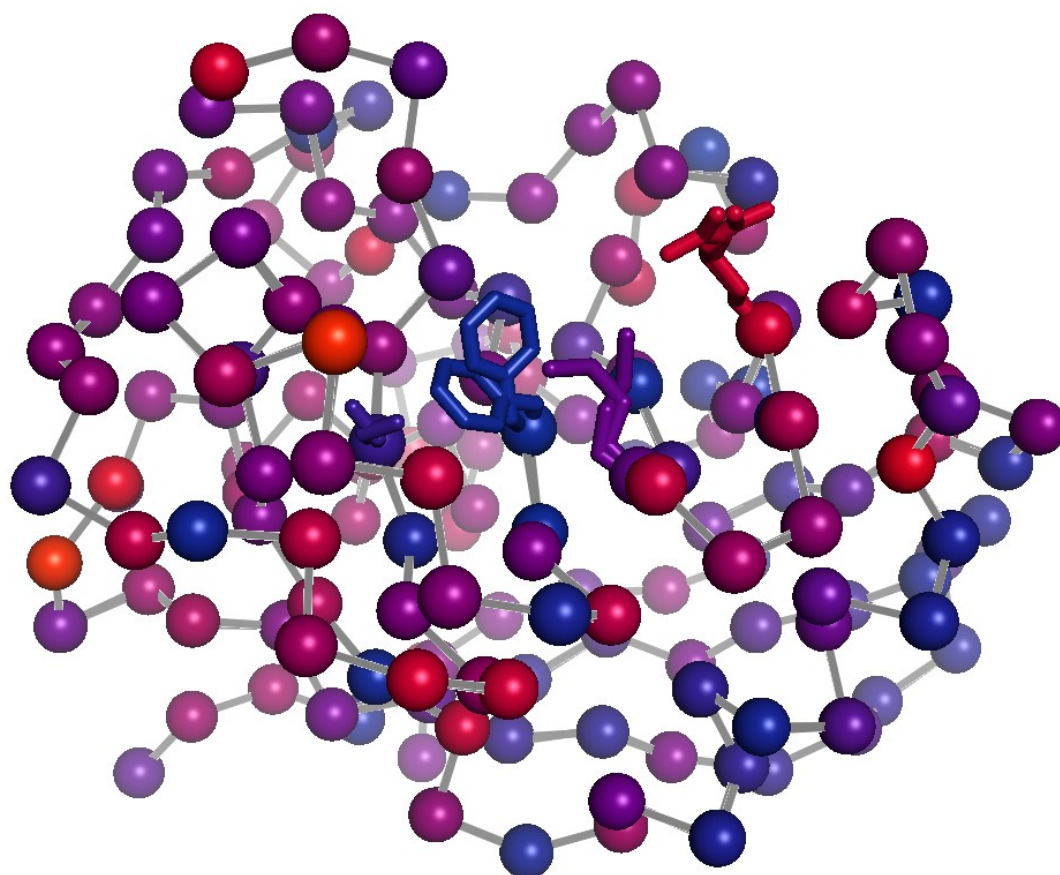
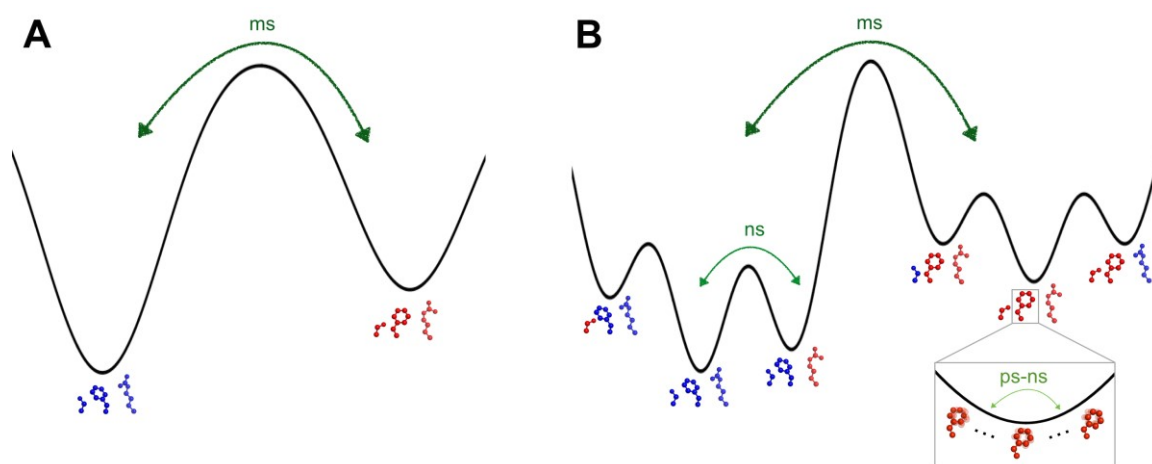900 **Movie 4**: 360˚ rotation around **Figure 7B**.
901

902

903   **Figure 8: The dynamic active-site network of CypA has a complex energy landscape. (A)** The previous
904   simple model in which Ser99, Phe113, and Arg55 (Met61 omitted for clarity) interconvert from one macrostate
905   (blue) to the other (red) completely collectively. NMR data suggest this process occurs on a millisecond
906   timescale. **(B)** A more nuanced model in which network microstates are populated differently depending on the
907   network macrostate, defined by the Phe113 rotameric state. In the left macrostate, Ser99 rotamer changes are
908   disfavored because of steric overlaps with Phe113, but Arg55 rotamer changes are accommodated; the reverse
909   is true (perhaps to a lesser extent) in the right macrostate. Within each microstate, rapid thermal motions occur
910   (bottom right), and may alleviate some minor steric overlaps. Timescales are estimates consistent with NMR
911   observables for CypA and other systems.

912

913